Engineering Structures 295 (2023) 116598

Contents lists available at ScienceDirect

Engineering Structures

journal homepage: www.elsevier.com/locate/engstruct

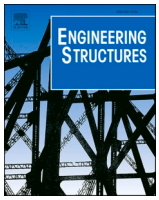

Experimental investigation of the shear response of large-scale fibre-reinforced concrete panels

Nicola Gehri [a,*], Jaime Mata-Falcón [a], Walter Kaufmann [a]

[a] Institute of Structural Engineering, ETH Zürich, Switzerland

ARTICLE INFO

Keywords:
Fibre-reinforced concrete
Shear behaviour
Large-scale testing
Panel experiments
Crack behaviour
Digital image correlation
Distributed fibre optical sensing
Post-peak instability

ABSTRACT

Although fibre-reinforced concrete has been the subject of extensive research for decades, its mechanical behaviour in shear is still not well understood. Furthermore, hardly any large-scale shear tests on elements with moderate fibre contents have been conducted to date. The present paper addresses this knowledge gap by presenting and discussing the results of an experimental campaign on large-scale fibre-reinforced concrete shear panels. Six panels with dimensions of 2.00 m × 2.00 m × 0.27 m were tested in the Large Universal Shell Element Tester at ETH Zurich by applying homogeneous shear. In four of these experiments, the in-plane shear was combined with homogeneous uniaxial compression by simulating the longitudinal restraint provided by the chords in a girder. Five tests focused on concrete of normal strength with moderate fibre contents and one test studied the behaviour of ultra high-performance fibre-reinforced concrete. The combined application of digital image correlation instrumentation and distributed fibre optical sensing allowed gaining a deeper insight into the structural behaviour of the panels. Overall, the test results showed the high efficiency of the fibres as shear reinforcement in large-scale web elements. However, failure of the panels without any steel reinforcing bars was rather brittle, with only few cracks forming over the element. The provision of a moderate amount of distributed longitudinal bar reinforcement has been found to be highly beneficial to the crack behaviour and thus significantly increase the ductility.

1. Introduction

For more than 50 years, the structural behaviour and the workability of fibre-reinforced concrete have been investigated in science and industry, with various concepts regarding concrete composition, fibre materials and geometry being developed [1,2]. While it is commonly accepted that adding fibres to concrete enhances the mechanical resistance and is beneficial for the crack behaviour of concrete structures in many cases, the application of fibre-reinforced concrete in industry is still essentially limited to slabs on grade and secondary elements such as façade elements, road pavements or (often temporary) tunnel linings [2]. The reason for this is the poor workability of fresh concrete at high fibre contents and the often insufficient load–deformation behaviour of fibre-reinforced concrete applications for moderately to heavily stressed elements when using more practical fibre contents [3].

Under tension, fibre-reinforced concrete with economical and practical fibre contents typically exhibits a softening behaviour after cracking, with the fibres being progressively pulled out of the concrete matrix. Such material behaviour typically leads to deformation localisation in individual cracks, resulting in brittle failures except in small-scale deformation-controlled experiments, where the post-cracking softening branch can be observed [1]. This lack of ductility is the main reason why concrete reinforced exclusively with fibres is hardly ever used in structural engineering today: unless very high unpractical fibre contents are used, fibres cannot replace conventional reinforcement ensuring structural safety under tensile load as they are unable to prevent failure at crack formation [2].

Fibres, however, have great potential as shear reinforcement, where a relatively low resistance of the transverse reinforcement is sufficient to prevent brittle shear failures if sufficient conventional longitudinal reinforcement is provided [4]. This is reflected in conventional reinforced concrete design, where the minimum transverse reinforcement in girders is typically less than a quarter of that required for ductile behaviour under tension [5,6]. Accordingly, a tensile strength corresponding to the reduced minimum reinforcement under shear load can thus already be ensured with moderate fibre contents [4]. Replacing conventional shear reinforcement by fibres can provide considerable economical and ecological benefits, as manual work for assembling and

* Corresponding author.
E-mail address: gehri@ibk.baug.ethz.ch (N. Gehri).

https://doi.org/10.1016/j.engstruct.2023.116598
Received 20 April 2023; Received in revised form 16 June 2023; Accepted 9 July 2023
Available online 18 September 2023

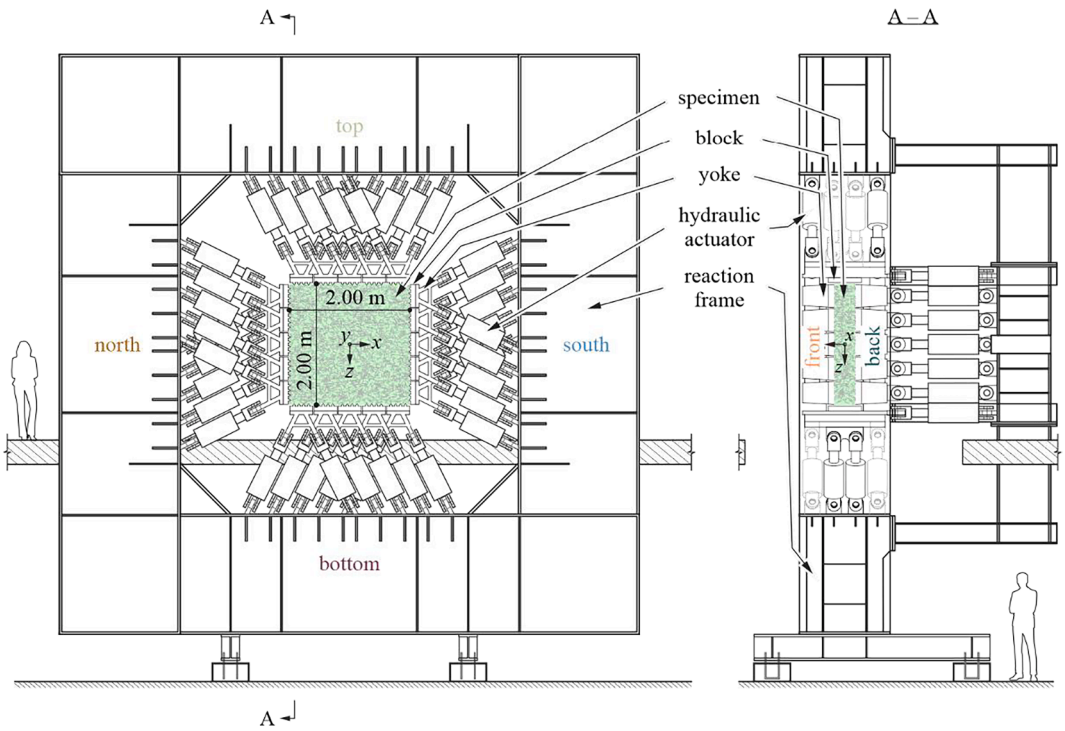

Fig. 1. Overview of the Large Universal Shell Element Tester (LUSET) with an installed panel: (a) elevation; (b) section A–A; adapted from [21].

placing the reinforcement is no longer necessary and resource-saving, thinner and variable web thicknesses become possible with considerably less effort [7].

Experiments on fibre-reinforced concrete beams without conventional shear reinforcement have already shown that brittle shear failures can be avoided by adding a certain amount of fibres, ensuring ductile flexural failures instead [8–13]. Li et al. [8] carried out one of the first series of tests on fibre-reinforced concrete beams without conventional shear reinforcement. They were able to show that the addition of fibres can considerably increase the shear resistance depending on the fibre content and material. These findings were confirmed a few years later by Adebar et al. [9], Kwak [10], Minelli [13] and Voo et al. [11] in their tests on similar beams. Parra-Montesinos [12] compiled a database of 147 steel fibre-reinforced concrete beam tests in 2006. His analysis led to the conclusion that deformed steel fibres could potentially replace conventional minimum shear reinforcement. He suggested performance criteria for the post-peak softening behaviour of the fibre-reinforced concrete mix and proposed a minimum fibre content of $\rho_{f,\min} = 0.75\%$ for beams without conventional shear reinforcement to guarantee a sufficient shear resistance "until further data become available". These performance criteria, and even more so the associated minimum fibre content, are purely empirical and presumably very conservative: The shear resistance of a beam with conventional minimum reinforcement according to the Swiss code for the design of concrete structures (SIA 262) [14], for example, is two to three times lower than the one obtained observing these requirements. The presumable conservatism of the requirements postulated by Parra-Montesinos [12] is justified, as they are not based on a mechanically consistent model [7]. However, the high minimum fibre content required is a severe limitation for the use of fibres as shear reinforcement in industry.

As with conventional reinforced concrete, beam shear tests alone cannot provide a sufficient experimental basis for the development and validation of mechanical models for fibre-reinforced concrete in shear, as the specimens differ significantly from most real structures in terms of size, loading and structural system [15]. Most importantly, due to the small depth of most beam shear test specimens – typically 5–10 times smaller than that of bridge girders – the shear force transferred by the web is uncertain since other load transfer mechanisms are important in small-scale specimens [16]. In addition, instead of the rectangular cross-sections frequently used in beam shear tests, profiled girders (e.g., T-beams and box girders) with stiff flanges controlling the longitudinal deformations of the web are common in practice [15]. Moreover, rather than concentrated loads as applied in common three- or four-point shear tests, uniformly distributed (dead) loads are dominant. Hence, large-scale experiments on the shear behaviour of fibre-reinforced membrane elements (such as webs of profiled beams) are essential to develop and validate mechanical models for fibre-reinforced concrete in shear. However, such tests are scarce, particularly regarding practical and economical fibre contents. To the authors' knowledge, the only shear panel tests with moderate fibre contents were conducted in the Shear Panel Tester at the University of Toronto [17–20] (in total, five tests with $\rho_f < 1\%$ are reported so far). They were tested in pure shear, being provided with very strong conventional bar reinforcement in the longitudinal direction distributed over the height of the element ($\rho_{s,x} = 3.31\%$) in addition to the fibres. This raises the question of how representative these tests are for elements of girder webs: The effect of the fibres as shear reinforcement is significantly influenced by the crack formation, which in turn is controlled by the longitudinal reinforcement. However, in real structures, such as bridge girders, the longitudinal reinforcement is primarily concentrated in the chords.

Hence, further experiments on fibre-reinforced panels are essential to build up a reliable and representative experimental database that can be used to develop and validate mechanical models. To this end, this paper presents an experimental campaign comprising six steel fibre-reinforced concrete shear panels aimed at representing bridge girder web elements in terms of size, reinforcement and loading conditions. The specimens measured 2.00 m × 2.00 m in plane, with a thickness of 0.27 m. The latter was deliberately chosen somewhat smaller than common in conventionally reinforced box girder bridge webs, as narrower dimensions are facilitated by the omission of conventional transverse reinforcement. The test series focused on moderate fibre contents as common in industry, aiming at replacing the conventional

Table 1
Overview of the experimental programme of the FS series: key parameters and material properties.

Specimen	Geometrical bar reinforcement ratios $\rho_x \mid \rho_z$[%]	Volumetric fibre content ρ_f[%] (Fibre dosage V_f [kg/m^3])	Cylinder compressive strength f_c: mean (CV) [MPa]	Residual flexural tensile strengths [(1)] $f_{R.1}$: mean (CV) [MPa] $f_{R.3}$: mean (CV) [MPa]	Loading (Monotonically increased control parameter)
FS1	0.94 | 0	0.51 (40)	50.3 (0.08)	5.7 (0.24) 5.9 (0.27)	pure shear (shear strain)
FS2	0.94 | 0	0.76 (60)	45.8 (0.05)	6.6 (–) 5.6 (–)	pure shear (shear stress)
FS3	0.28 | 0	0.51 (40)	49.5 (0.08)	4.4 (0.21) 4.9 (0.37)	shear with restrained longitudinal deformation (shear strain)
FS4	0 | 0	0.51 (40)	46.4 (0.03)	3.1 (0.16) 3.5 (0.12)	shear with restrained longitudinal deformation (shear strain)
FS5	0 | 0	0.76 (60)	48.3 (0.05)	5.3 (0.30) 4.9 (0.25)	shear with restrained longitudinal deformation (shear stress)
FS6 (UHPFRC)	0 | 0	3.35 (263)	169.9 (0.10)	11.0 (0.15) 9.5 (0.05)	shear with restrained longitudinal deformation (shear strain)

[(1)] Determined by three-point bending tests on notched prisms according to EN 14651 [24] at crack mouth opening displacements $CMOD_1 = 0.5$ mm and $CMOD_3 = 2.5$ mm, respectively: Only the results from specimens with a cut surface at the tension side were considered.

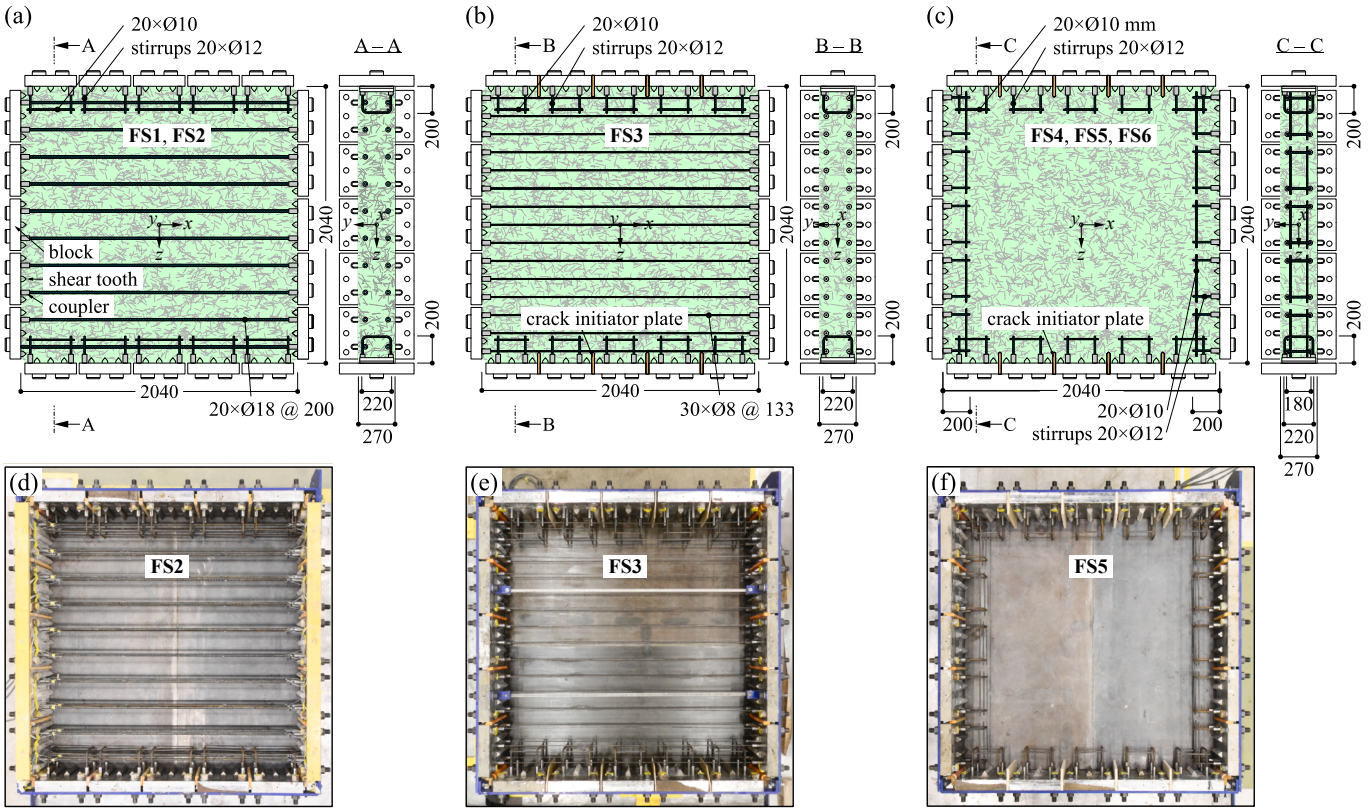

Fig. 2. Panel geometry and reinforcement layout of the FS series (dimensions in mm): (a) FS1 and FS2; (b) FS3; (c) FS4, FS5 and FS6; photographs of the specimens before casting: (d) FS2; (e) FS3; (f) FS5.

minimum shear reinforcement in girder webs made of normal-strength concrete. The tests were conducted in the Large Universal Shell Element Tester (LUSET [21]) at ETH Zurich. The experimental procedure is outlined in Section 2, which covers the design of the specimens, the test setup, the loading, the details of the instrumentation and the companion material tests. The experimental results are presented, analysed and discussed in Section 3. To this end, the experimental data are thoroughly examined with respect to several aspects: On the one hand, the influence on the structural behaviour of the main experimental parameters (i.e. the loading conditions, the longitudinal bar reinforcement ratios and the fibre contents) is studied, and on the other hand, the post-peak stability of the tests is addressed. Based on these observations, preliminary recommendations for the replacement of conventional shear reinforcement by steel fibres are given.

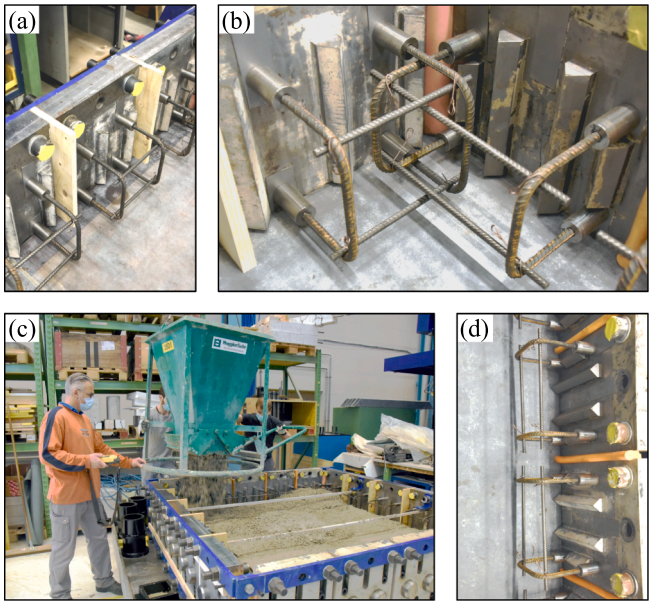

Fig. 3. Details of production of the specimens: (a) crack initiator plates and edge reinforcement at the top edge of the specimen; (b) edge reinforcement at a corner; (c) casting of specimen; (d) north edge reinforcement.

2. Experimental campaign

2.1. Overview

In this study, six shear tests on fibre-reinforced concrete panels with dimensions of 2.00 m × 2.00 m × 0.27 m were conducted. The tests differed in the volumetric steel fibre content (ρ_f), the geometrical reinforcement ratio of the longitudinal bars ($\rho_{s,x} \in \{0, 0.28, 0.94\}$%) and the loading conditions. No test contained conventional transverse reinforcement ($\rho_{s,z} = 0$). Five tests were carried out on elements of normal-strength concrete with moderate amounts of fibres ($V_f \in \{40, 60\}$kg/m$^3 \triangleq \rho_f \in \{0.51, 0.76\}$%). These tests aimed at investigating the potential of fibre reinforcement as a replacement for the conventional minimum shear reinforcement in webs of girders. The minimum fibre dosage in the tests was designed to provide the same shear resistance as a 0.2% conventional shear reinforcement. This amount of reinforcement was proposed by Beck [15] as the minimum transverse reinforcement in webs of large girders without fibres. The shear resistance of the fibres was quantified using the fibre effective stress described by Pfyl, assuming a 3D fibre distribution with a lower limit angle of effective fibres of 60° [1]. This design resulted in a minimum fibre dosage of 40 kg/m^3. Additionally, one test on an ultra high-performance fibre-reinforced concrete (UHPFRC) panel was carried out to assess the structural behaviour in comparison to the conventional steel fibre-reinforced specimens. In parallel, material tests were carried out to determine the relevant material characteristics (see Sections 2.2 and 2.3).

The six experiments denominated FS1–FS6 ("*F*ibre-reinforced concrete in *S*hear") were produced in the structural laboratory at ETH Zurich and tested in the Large Universal Shell Element Tester (LUSET, [21,22]; Fig. 1). The test setup is explained in more detail in Section 2.4.

The experimental programme and the key parameters are summarised in Table 1. In order to investigate the fundamental structural behaviour of the elements and provide an experimental basis for the development and validation of mechanical models of fibre-reinforced concrete, it was chosen to apply homogeneous in-plane loading. Four of the tests were loaded in homogenous in-plane shear with restrained longitudinal deformation (generating longitudinal compression), either without (three tests including the UHPFRC specimen) or with light (one test) longitudinal bar reinforcement. This configuration was chosen to represent an element of a typical prestressed concrete girder web, where (i) the longitudinal bar reinforcement is primarily concentrated in the chords and (ii) the stiff (prestressed) chords control the longitudinal deformations of the web. The mean longitudinal deformations of the panels were controlled to zero during the test by applying homogeneous longitudinal compression to the panels. It should be noted that this longitudinal restraint (i) was controlled using the actuator strokes and hence included the deformations of the LUSET (see Section 2.5) and (ii) differs from a real prestressed girder web element, which is initially compressed and expands slightly under load. The other two specimens were loaded in pure homogeneous in-plane shear but provided with a significant longitudinal bar reinforcement distributed over the element height. This configuration was chosen to facilitate the comparison with earlier tests at other universities, where longitudinal reinforcement was provided rather than controlling the longitudinal deformations of the elements. These tests targeted the assessment of the influence of the distributed longitudinal bar reinforcement and the loading on the structural behaviour of the panels. The details of the loading configuration are given in Section 2.6.

All six specimens were instrumented with state-of-the-art measurement technology [23], which made it possible to comprehensively measure quasi-continuous strains along the reinforcing bars (distributed fibre optical strain measurements) and deformations on the surface (3D digital image correlation) in all tests (see details in Section 2.5).

2.2. Specimens

Fig. 2 illustrates the geometry (identical) and reinforcement layout of all six specimens FS1–FS6. The effective edge dimensions of the panels were 2.00 m × 2.00 m, with the theoretical edges corresponding to the intersection points of the in-plane actuator axes per yoke; note that the total casting width of 2.04 m was slightly larger due to the load introduction through the 40 mm wide shear teeth of the load introduction blocks [21]. The thickness of all panels was 0.27 m. No specimen contained transverse (vertical) reinforcing bars ($\rho_{s,z} = 0$). The longitudinal (horizontal) geometrical bar reinforcement ratio was $\rho_{s,x} = 0.94$% for Specimens FS1 and FS2 (Ø18 mm reinforcing bars, spacing $s = 200$ mm, double-layered) and $\rho_{s,x} = 0.28$% for FS3 (Ø8 mm, $s = 133$ mm, double-layered); FS4–FS6 contained no reinforcing bars ($\rho_{s,x} = \rho_{s,z} = 0$). The longitudinal reinforcing bars were connected to steel blocks (used to mount the specimens in the LUSET and distribute the applied loads, see Fig. 1) by means of reinforcing bar couplers fixed to the blocks with M24 high-strength bolts. At the yokes without connected bar reinforcement (top and bottom yokes, as well as north and south yokes in specimens without longitudinal bar reinforcement), the shear force transfer from the blocks to the fibre-reinforced concrete through the shear teeth was facilitated by providing Ø12 mm edge stirrups bolted to the blocks via couplers and Ø10 mm short straight reinforcing bars placed parallel to the specimen edge in the corners of the stirrups (see Fig. 2 and Fig. 3). This edge reinforcement provided a mechanical anchorage of the individual blocks to the specimen, avoiding edge failures while interfering minimally with the overall behaviour of the panel. A similar concept of mechanical anchoring was successfully used in experiments on fibre-reinforced concrete shear panels in the Shear Panel Tester of the University of Toronto [17–20]. In FS3–FS6, timber plates between the blocks were installed at the top and bottom edges of the specimens every 400 mm (Fig. 2(b) and (c) and Fig. 3(a)) as crack initiators. They aimed at simulating the formation of shear cracks in the web that are typically triggered by the progression of cracks formed in the tension chord.

The specimens were prepared and cast on two vibrating casting tables in the Structures Laboratory of ETH Zurich (see Fig. 3(c)). Although a vertical casting would have been more representative of typical web elements in practice, the specimens were cast horizontally for practical

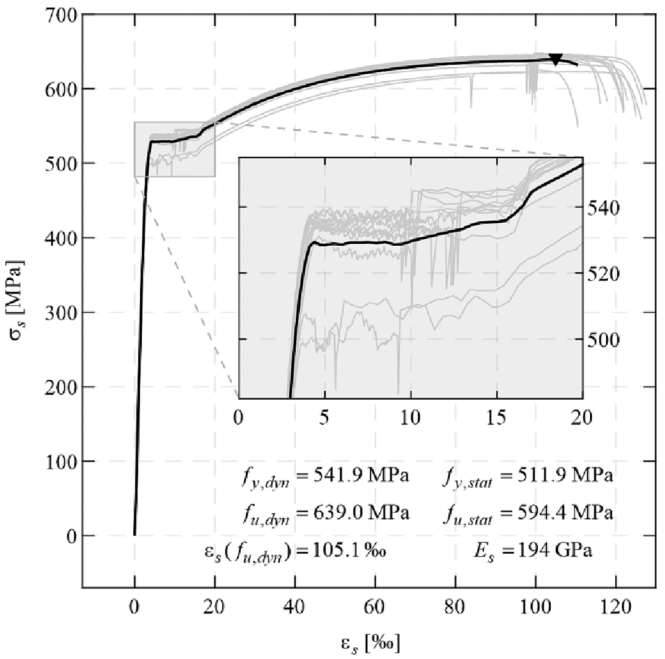

Fig. 4. Stress–strain diagrams of the longitudinal reinforcing bars Ø18 in FS1 and FS2, with the individual samples plotted in grey and the mean response in black (the triangle indicates the dynamic tensile strength).

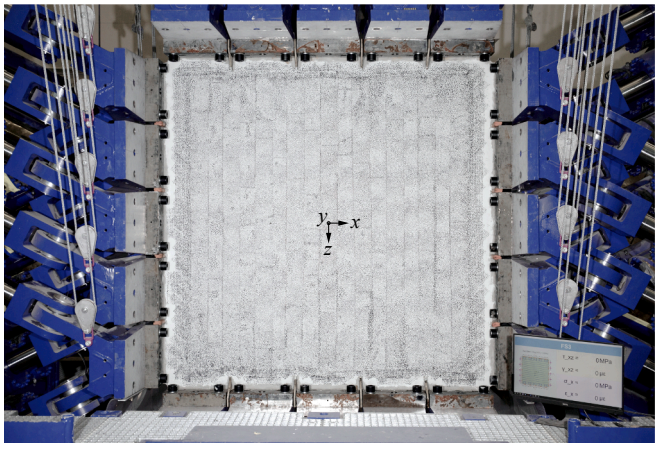

Fig. 5. A specimen (FS3) installed in the Large Universal Shell Element Tester (LUSET) before testing; view from the front.

and economical reasons. It should be noted that the casting direction affects the fibre distribution and orientation in the concrete, which may influence the mechanical behaviour.

For FS1–FS5, the fibre-reinforced concrete mix was produced at a batching plant and delivered by a truck mixer. FS1/3 and FS2/5, respectively, were cast together from the same batch. For FS6, a ready-mix ultra high-performance fibre-reinforced concrete was produced in the laboratory with the support of a product supplier expert. All specimens were poured with a bucket in two stages. Vibration on the casting table was applied in each layer to ensure a proper concrete compaction. Special care was taken to prevent excessive vibration potentially causing segregation of the aggregates and fibres. After finishing the concrete surface, the specimens were covered with a plastic foil for at least three days and left to cure in the laboratory. Parallel to the panels, the specimens for the material characterisation were produced (see Section 2.3.1). The panels were tested between 27 and 84 days after casting.

2.3. Materials

2.3.1. Fibre-reinforced concrete

For FS1–FS5, a conventional normal-strength concrete C30/37 with a maximum aggregate size of 16 mm was used. The fibres used in these tests were Dramix® 3D 80/60 BG hooked-end steel fibres of length l_f = 60 mm and diameter d_f = 0.75 mm supplied by the company N.V. Bekaert SA [25]. The specified nominal tensile strength of the fibres was 1225 MPa. FS6 was made from Ductal® ultra high-performance fibre-reinforced concrete (UHPFRC) of class UA according to the Swiss guideline SIA 2052 [26] and supplied by the Holcim (Switzerland) SA. This mix contained short straight metallic fibres of length l_f = 20 mm and diameter d_f = 0.2 mm. The fibre contents are provided in Table 1.

For each panel experiment, the uniaxial concrete compressive strength f_c and the residual flexural tensile strengths $f_{R,j}$ of the fibre-reinforced concrete were determined (see mean results and coefficients of variation (CV) in Table 1). These companion material tests were conducted at the same time as the panel experiments. The uniaxial compressive strengths f_c were obtained by cylinder compression tests. The residual flexural tensile strengths $f_{R,j}$ were determined by three-point bending tests on notched beams according to EN 14651 [24]. Two approaches were used to produce the beam specimens for these tests. Besides following the production procedure specified by EN 14651 (i.e. casting specimens in individual moulds), some samples were cut from elements to better represent the dimensions of the panel. This allowed studying the effect of boundary surfaces on the dispersion and orientation of the fibres in the concrete. In general, the results from the bending tests – in combination with manual fibre counting in the failure planes – showed that the beams with a formed surface at the tension side overestimate the strength due to the boundary effect. Consequently, exclusively the results from beams with a cut surface at the tension side were considered in the evaluation of the residual flexural tensile strengths $f_{R,j}$ indicated in Table 1. Note that three-point bending tests were also carried out on FS6 to maintain consistency in the testing procedure, despite the fact that four-point bending tests on un-notched beams are commonly used for the material characterisation of UHPFRC. Complete information on the fibre-reinforced concrete companion material tests is provided in Appendix A.

2.3.2. Reinforcing bars

All reinforcing bars were deformed steel of Class B500B. The longitudinal Ø18 mm reinforcing bars in FS1 and FS2 were from the same production batch for both specimens. Uniaxial tension tests were carried out for these bars at a strain rate of 0.01%/s to determine the stress–strain response. The results of the 12 tension tests (in grey) and the mean stress–strain response (in black) are shown in Fig. 4, along with the mean static and dynamic steel characteristics determined as proposed by Häfliger et al. [27,28]. Note that the static values $f_{y,stat}$ and $f_{u,stat}$ were determined by stopping the deformation-controlled loading for 2 min after reaching the yield stress and close to the tensile strength, respectively. No material tests were conducted for the reinforcing bars of the edge reinforcement nor the light longitudinal reinforcement in FS3.

2.4. Test setup

The six experiments were conducted in the Large Universal Shell Element Tester (LUSET) [21]. The specimens were installed in the LUSET through the steel blocks that were connected to the loading yokes of the LUSET by M36 high-strength bolts, see Fig. 5. The shear transfer between the yokes and the blocks was ensured by shear keys (cylindrical part protruding from outer block edge and corresponding hole in yoke). Each of the twenty yokes is controlled by five hydraulic actuators that are connected to the reaction frame of the LUSET (see Fig. 1). In its standard configuration used for these tests, the LUSET is actuated by twenty servo-hydraulic valves, where each valve is connected to one

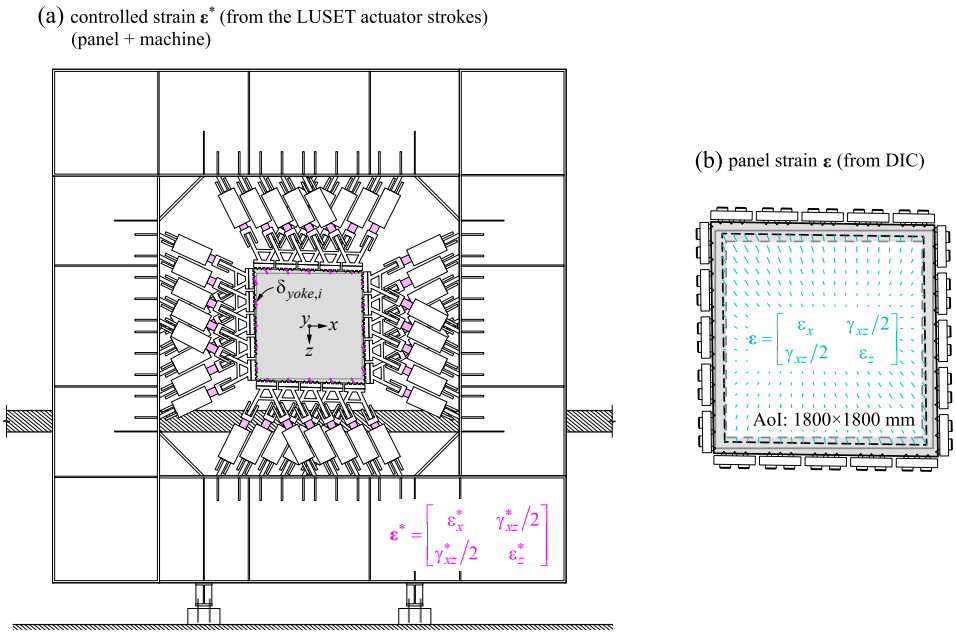

Fig. 6. Definitions of strains: (a) LUSET strain $\boldsymbol{\varepsilon}^*$ computed as the best-fit homogeneous panel deformation based on the actuator strokes of the LUSET (used as control variables, includes the LUSET deformations); (b) DIC strain $\boldsymbol{\varepsilon}$ computed as the best-fit homogenous panel deformation based on the full-field DIC measurements (used in the post-processing, not biased by the LUSET deformations).

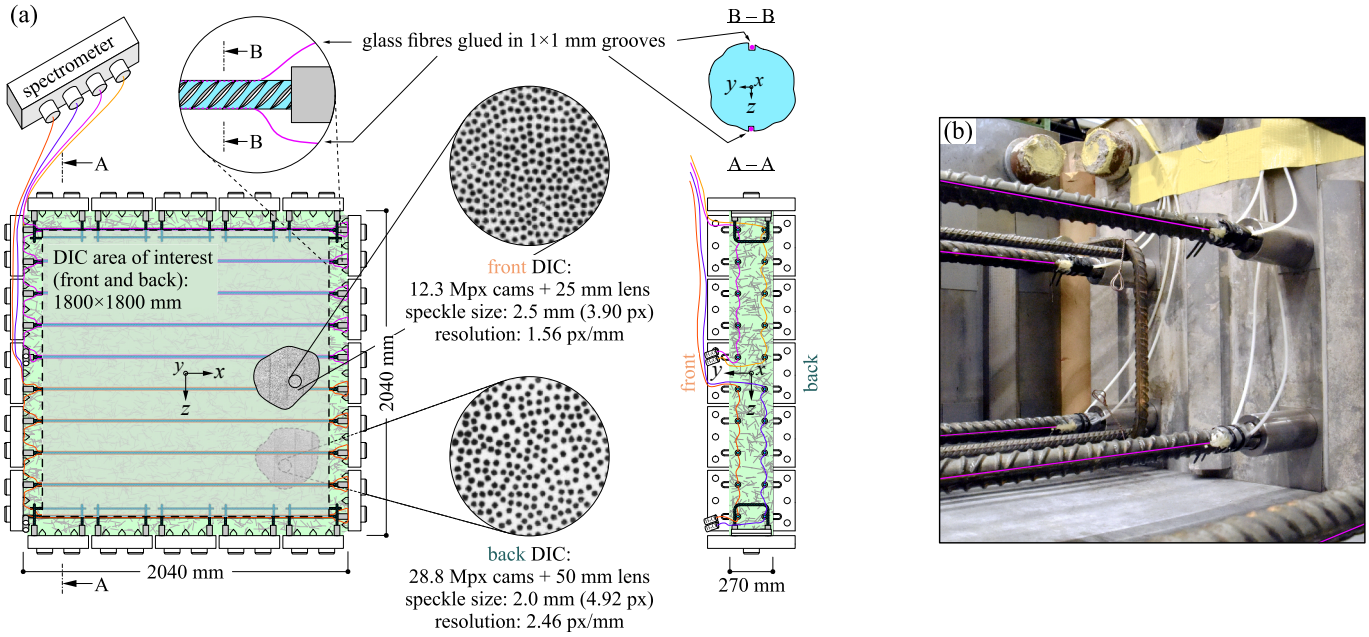

Fig. 7. Instrumentation: (a) details of the DIC setup on the front and back side of the specimens and the fibre optical strain sensing system of the reinforcing bars in FS1 and FS2; (b) optical glass fibres glued in opposing grooves carved in the reinforcing bars (highlighted in magenta), with adjacent transition zone where the fibres continue in protective tubes out of the specimen. (For interpretation of the references to colour in this figure legend, the reader is referred to the web version of this article.)

layer of five parallel actuators per edge. Hence, except for potential differences in frictional forces, the five yokes per edge apply the same load and allow the element to be loaded homogeneously (for more details, see [21]). The relevant details of the built-in measuring devices of the LUSET, as well as the control system and the resultant applied loading, are described in Sections 2.5 and 2.6.

2.5. Instrumentation

The LUSET is instrumented with built-in real-time measurement elements, which were also used to control the experiments via the servo-hydraulic valves. It consists primarily of the displacement and force measurements of each actuator by means of internal displacement transducers and load pins, respectively. A Lagrangian optimisation was

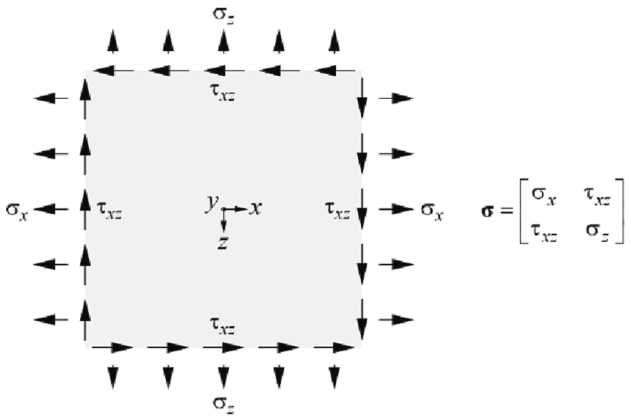

Fig. 8. Homogeneous loading in the LUSET by in-plane forces and its representation with the nominal plane stresses σ_x, σ_z and τ_{xz}.

used to reduce the noise of the sensors [29]. As will be described more in detail in Section 2.6, several stress resultants of the element were controlled in all tests and, except for FS2, at least one component of the panel deformation was additionally controlled. The controlled panel deformation was the best-fit homogeneous plane strain $\boldsymbol{\varepsilon}^*$ of the specimen determined based on the displacement measurements of the actuators. To this end, the displacement of each yoke $\delta_{yoke,i}$ was computed first using the displacement measurements of the five actuators that load the corresponding yoke. Subsequently, $\boldsymbol{\varepsilon}^*$ was determined from the twenty yoke displacements $\delta_{yoke,i}$, $i \in \{1, 2, \ldots, 20\}$ (see Fig. 6(a); more details on the computation of $\boldsymbol{\varepsilon}^*$ are provided in Appendix B.1). Note that the controlled strain $\boldsymbol{\varepsilon}^*$ was not corrected to account for the machine stiffness, which is highly non-linear, depends on the loading type and is influenced by various parameters (stiffness of the reaction frame and the load introduction elements, slip of the pins at the actuator joints, etc.) [15]. Hence, the controlled strain $\boldsymbol{\varepsilon}^*$ includes – besides the panel deformation – the deformations of the LUSET. Controlling the LUSET with a real-time measurement system that directly measures (unbiased) specimen deformations would be advantageous but is not available to date (see discussion in Section 3.5).

In addition to the aforementioned built-in measurement elements of the LUSET, independent optical measurement systems were applied to investigate the load–deformation behaviour of the elements (Fig. 7). Two three-dimensional Digital Image Correlation (DIC) systems (VIC-3D from Correlated Solution [30]) were used to measure the full-field quasi-continuous deformations of the front and back surfaces of the specimen (Fig. 7(a)). Both surfaces were prepared with white priming and a black speckle pattern to achieve maximum contrast. The front surface was instrumented with a pair of 12.3 Mpx FLIR Grasshopper 3 cameras with 24 mm lenses from Schneider-Kreuznach and the back surface with a pair of 28.8 Mpx Prosilica GT 6600 cameras with Zeiss lenses of 50 mm focal length. The area of interest of the DIC systems covered 1800 mm × 1800 mm on both sides.

The cracks formed during the tests and their kinematics were automatically detected and measured using the Automated Crack Detection and Measurement software (ACDM) [31,32]. Additionally, the measured surface deformations were processed according to [31] to obtain the best-fit homogeneous in-plane strain $\boldsymbol{\varepsilon}$ of the panel (see Fig. 6 (b)). The two DIC setups are shown in Fig. 7(a). Details on the DIC and ACDM parameters and estimation of the measurement uncertainty are provided in Appendix B.2.

All longitudinal Ø18 mm reinforcing bars in FS1 and FS2 were instrumented with a distributed fibre optical sensing (DFOS) system (Odisi 6104 from Luna Innovations Inc. [33]), allowing to measure quasi-continuously the strain of the bars along their length (see Fig. 7). For this purpose, bend-insensitive polyimide-coated single-mode fibres (type SM1250B3[9.8/125]P) were glued in small grooves with a cross-section of 1 mm × 1 mm carved along the reinforcing bars. At both ends of the glued fibre section was a transition zone, where the glass fibres leave the grooves and continue in protective tubes out of the specimen. The instrumented length of each bar was thus 1.7 m. The fibre optical sensor installation, the data acquisition and the post-processing followed the best practice recommendations given in [23,34,35].

Each reinforcing bar was instrumented with two opposing fibre optical sensors (at the top and bottom of the bar), enabling the measurement of the bar curvature in addition to the axial strain. The strain measurements were converted to normal forces, bending moments and shear forces of the reinforcing bars by following the methods proposed in [34,35]. To this end, the reinforcing bars were idealised as uniaxial Euler–Bernoulli beams, whose strain planes are uniquely defined by the two strain measurements at the top and bottom of the bar. The stress distributions in the bar cross-section were calculated by using the stress–strain relationship illustrated in Fig. 4. Integration of the stresses over the cross-section provided the normal forces F_s and bending moments M_s acting on the bar. Finally, the shear forces were obtained as the derivatives of the bending moments with respect to the longitudinal coordinate, i.e. $V_s = dM_s/dx$.

2.6. Loading

All panels were subjected to quasi-static homogeneous membrane forces (stress resultants n_x, n_z and n_{xz}), represented in the following by the nominal plane stresses σ_x, σ_z and τ_{xz} (see Fig. 8) obtained by dividing the stress resultants by the nominal element thickness. FS1 and FS2 were loaded in pure shear, while FS3–FS6 were loaded in shear with the mean longitudinal deformation of the panel being controlled to zero, which was achieved by applying homogeneous longitudinal compression $-\sigma_x$ on the panel (see Fig. 9). As outlined in Section 2.5, the controlled panel deformation was the best-fit homogeneous strain $\boldsymbol{\varepsilon}^*$ of the specimen determined based on the displacement measurements of the actuators and thus included also the deformations of the LUSET. Hence, although in FS3–FS6 the longitudinal deformation was controlled to zero ($\varepsilon_x^* = 0$), it was expected that the specimen would slightly expand longitudinally due to the deformations of the LUSET ($\varepsilon_x \geq 0$). These horizontal strains of the specimen were accepted as they essentially correspond to the longitudinal strains in the web of a prestressed girder, which also expand slightly under increasing load.

Apart from the nominal shear stress τ_{xz}, and the nominal longitudinal stress σ_x in FS3–FS6, all other in-plane and out-of-plane stress resultants were kept at zero during the test and a rigid motion of the specimen was prevented by the controller. In all tests, three of the total six variables (σ_x, σ_z, τ_{xz}, ε_x^*, ε_z^*, γ_{xz}^*) describing the in-plane stress state and the deformations of the panel were controlled (indicated in Fig. 9 with the increased variable in magenta and the two variables controlled to zero in red). The other three variables resulted from the load–deformation behaviour of the panel.

At the beginning of the tests, the forces of all actuators were controlled to zero. FS2 and FS5 were loaded by monotonically increasing the nominal shear stress τ_{xz}; in FS5, an additional longitudinal compression $-\sigma_x$ developed due to the restrained longitudinal deformation of the panel. The other four tests (FS1, FS3, FS4 and FS6) were loaded by monotonically increasing the shear deformation of the panel γ_{xz}^*. The latter loading control module was developed during the test series (after conducting FS2 and FS5) to capture the post-peak load–deformation behaviour of the panels after reaching their maximum shear stress $\tau_{xz,ult}$ and to be able to investigate the failure mechanism in more detail. The loadings were applied quasi-statically with rates of $d\tau_{xz}/dt \approx 0.03$ MPa/min in FS2 and FS5, $d\gamma_{xz}^*/dt \approx 50 \times 10^{-6}$/min in FS1, FS3 and FS4, and $d\gamma_{xz}^*/dt \approx 100 \times 10^{-6}$/min in FS6.

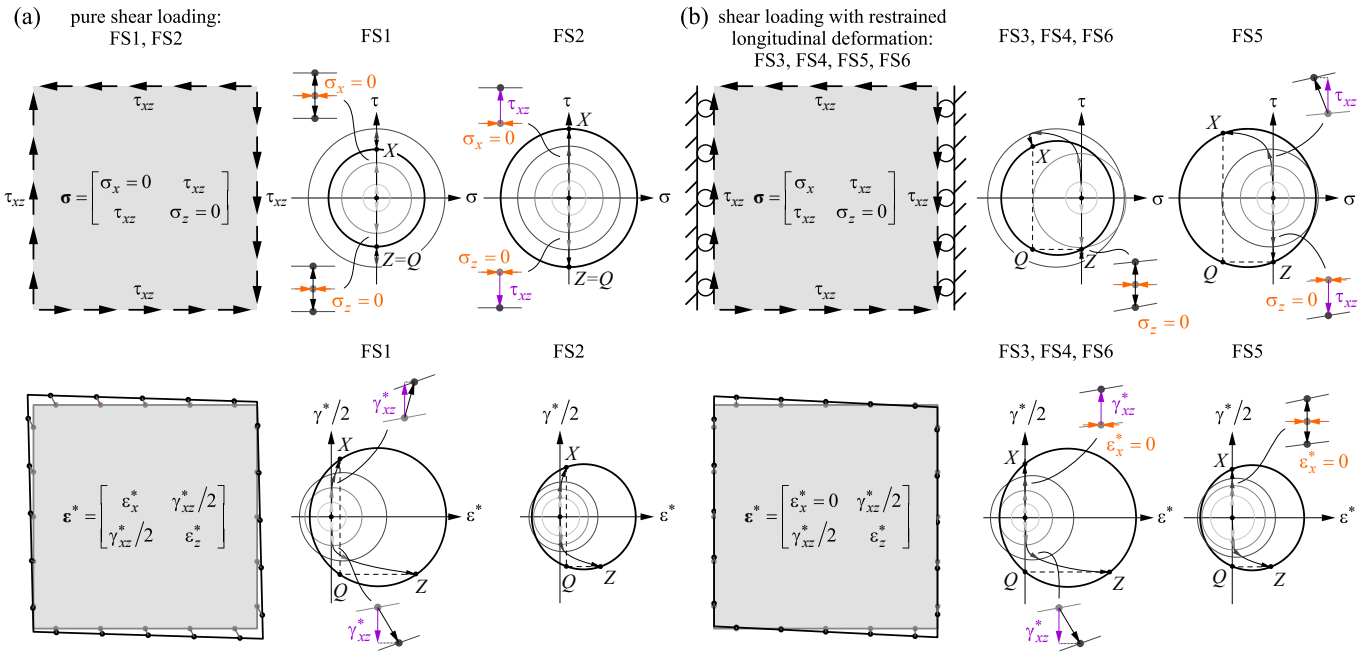

Fig. 9. Loading of the specimens: stress states (top) and deformations (bottom) of the panels subjected to (a) pure shear loading (FS1 and FS2) and (b) shear loading with restrained longitudinal deformation (FS3 to FS6). The Mohr's circles of stresses and strains qualitatively indicate the loading path of each experiment (orange = two variables controlled to zero in each experiment, purple = monotonically increased control variable). (For interpretation of the references to colour in this figure legend, the reader is referred to the web version of this article.)

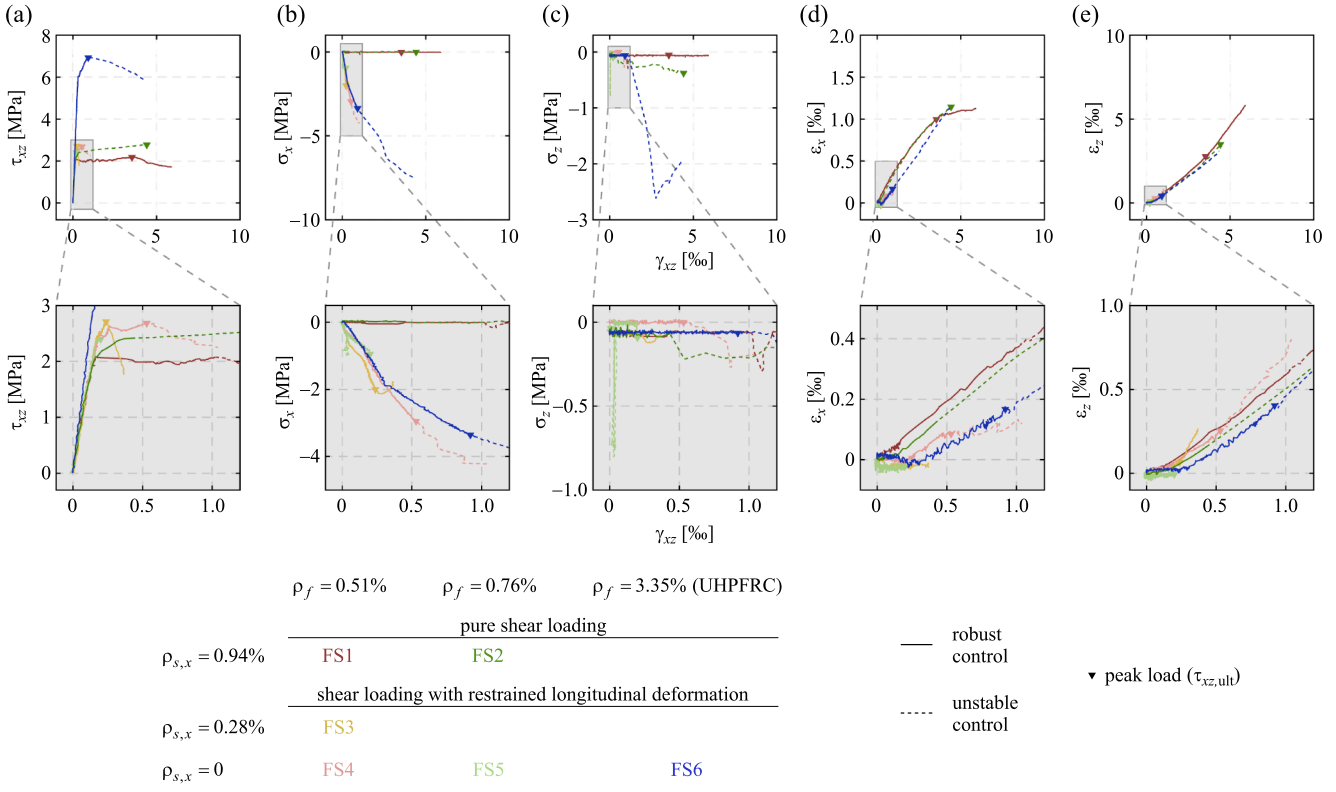

Fig. 10. Load–deformation behaviour of FS1–FS6: (a)–(c) nominal stresses (τ_{xz}, σ_x,σ_z) and (d)–(e) axial strains (ε_x, ε_z) as functions of the shear strain γ_{xz} (bottom row shows details of shaded regions in top row).

3. Experimental results and discussion

3.1. General remarks on the test protocol

The structural responses of FS1–FS6 are summarised in Fig. 10 with the shear strain γ_{xz} on the abscissae and the nominal stresses ($\tau_{xz}, \sigma_x, \sigma_z$) and axial strains ($\varepsilon_x, \varepsilon_z$) on the ordinates. Note that the strains of the panels were derived from the digital image correlation (DIC) measurements at the front and back surface of the specimen as the average of the two corresponding best-fit homogeneous strains. The detailed loading histories in Appendix C show that the deviations of the strains between the two sides were marginal, indicating that the through-thickness variations of the deformations can be neglected. The loading path and boundary conditions defined in Section 2.6 could be followed with only a few exceptions that are discussed in the following.

As described in Section 2.5, the panel strains differ from the controlled strain. $\boldsymbol{\varepsilon}^*$, which also includes the deformations of the Large Universal Shell Element Tester (LUSET). The shear deformations of the LUSET (see the differences between γ_{xz} and γ^*_{xz} in Appendix C) were shown to be larger than the shear deformations of the panel itself, which indicates a lower stiffness of the testing machine in comparison to the panels even after crack formation.

The two shear stress-controlled specimens (FS2 and FS5) were tested until the peak shear stress was reached. Due to issues with the control system, the LUSET shut down twice during testing of FS5. Fortunately, the shutdowns were in the early stage of loading, with the panel still being uncracked; thus, reloading to the state before the shutdown worked well without affecting the failure behaviour. Additionally, undesired vertical stresses σ_z occurred in FS2 and FS5 at crack formation. This is a known phenomenon in force-controlled panel tests in the LUSET, which occurs due to the instant expansion of the specimen at cracking. Since the actuator (stroke) velocities are limited for safety reasons, the test setup needed a certain time to react and accommodate this expansion, hence vertical compression built up in a first instant. However, beyond the peak load this compression could not be reduced to zero as the shear stress was controlled to gradually increase at the specified rate, resulting in a rapidly growing crack pattern of the specimens that even amplified this effect. In FS5, this led to a brittle premature failure of the specimen at first cracking, whereas in FS2 the shear stress could still be slightly increased after first cracking but without the vertical compression being relieved.

Only the shear strain-controlled loading used in the four other tests (FS1, FS3, FS4 and FS6) enabled testing of the post-peak behaviour of the panels. In addition, it allowed the specimens to be tested more robustly during cracking. Crack occurrence in these tests resulted in drops of the shear stresses, similarly as observed in tests with simpler loading configurations. FS1 and FS3 were successfully loaded into the post-peak range and were stopped at wide cracks of several centimetres. In FS4 and FS6, undesired vertical stresses σ_z and deviations among the shear stresses τ_{xz} at the four edges of the panel occurred shortly after reaching the peak shear stress with limited distributed cracking. Additionally, the specified shear strain rates in FS4 and FS6 were not met from this point on. These control issues arose due to the aforementioned low shear stiffness of the LUSET, which led to structural instabilities of FS4 and FS6 (studied in detail in Section 3.5). In Fig. 10, the final part of the tests where substantial deviations from the prescribed loading paths and boundary conditions arose due to instabilities in the control system are indicated by dashed lines.

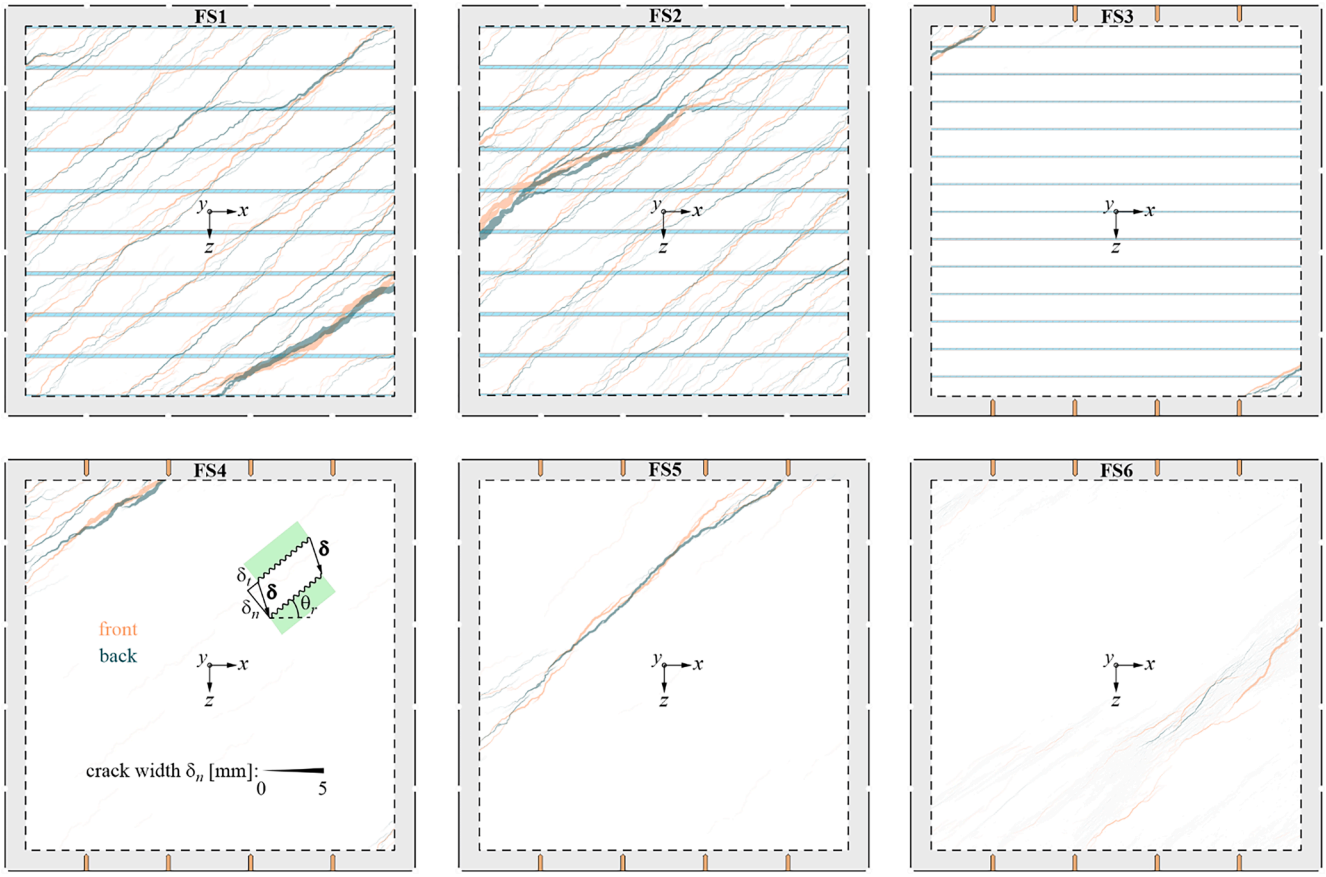

Fig. 11. Overlaid crack patterns of the front and back surface of the specimens FS1–FS6 at the peak load with the line thickness proportional to the crack widths.

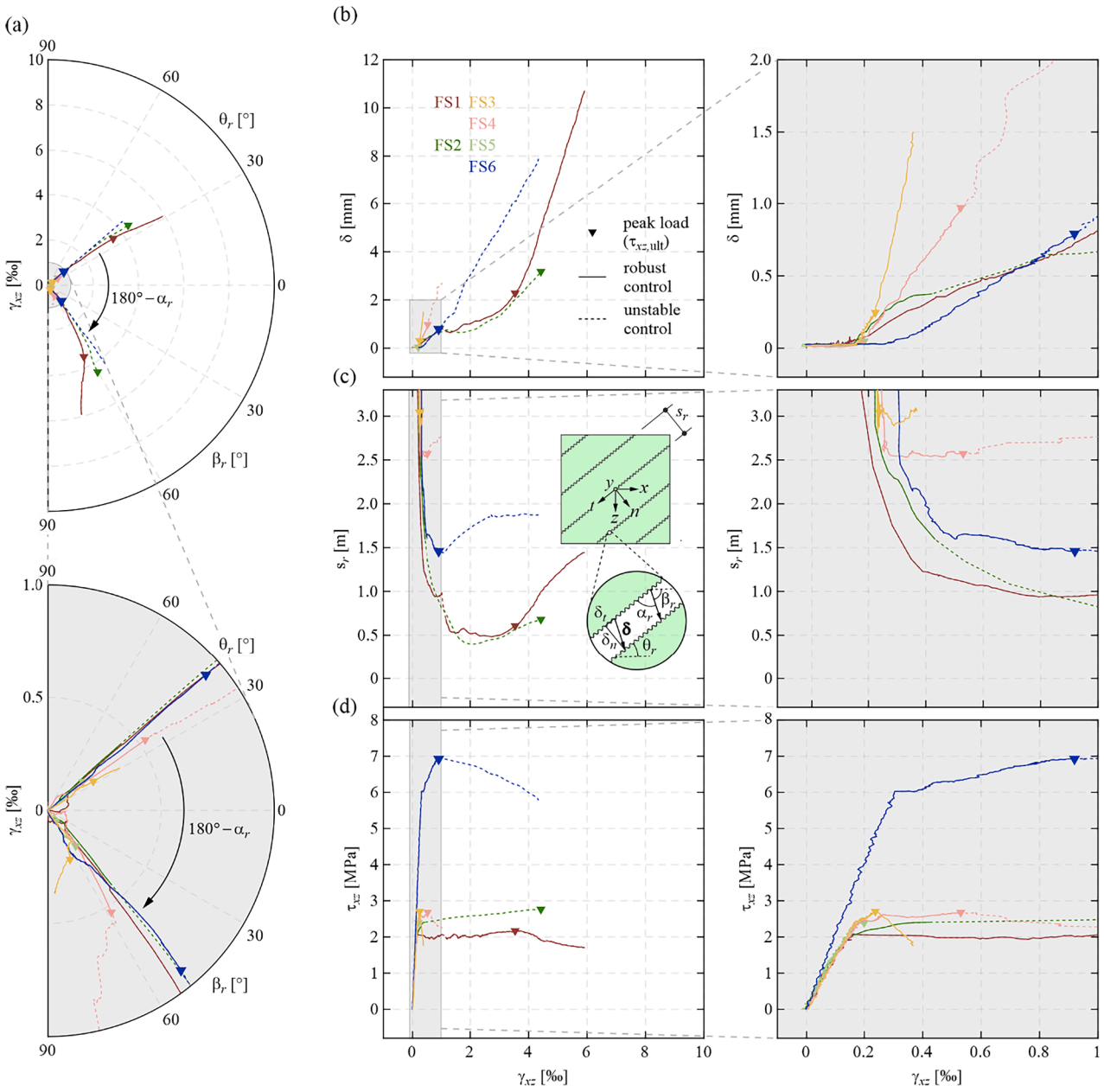

Fig. 12. Behaviour of the equivalent homogeneous cracks of FS1–FS6: (a) the characteristic crack displacement magnitude δ and direction β_r with respect to the x-axis; (b) characteristic crack inclination θ_r; (c) characteristic crack spacing s_r (the nominal shear stress–strain behaviour presented in Fig. 10 is included in the (d) for direct comparison).

3.2. Load–deformation behaviour

The structural responses of FS1–FS6 shown in Fig. 10 can be described by three distinct ranges in the nominal shear stress τ_{xz}–shear strain γ_{xz} domain: (i) a stiff linear elastic range up to cracking, (ii) a hardening range with the formation of multiple cracks up to the peak nominal shear stress ($\tau_{xz,ult}$), and (iii) a softening range with reducing shear stress at increasing shear strain and where a crack localises. Note that the latter range could only be tested in the shear strain-controlled experiments (FS1, FS3, FS4 and FS6). The complete experimental data are shared in a public data repository (see corresponding section).

The uncracked range (i) was almost identical in all experiments. Only FS6, which was made from ultra high-performance fibre-reinforced concrete (UHPFRC), exhibited a slightly higher uncracked stiffness. In the hardening range (ii) of FS1 and FS2, which both contained longitudinal bar reinforcement and were tested in pure shear, large shear strains γ_{xz} (3.5 and 4.4‰ for FS1 and FS2, respectively) at almost constant nominal shear stress τ_{xz} were observed. In both tests, several diagonal cracks, distributed over the element, formed before reaching the peak load (see crack behaviour description in Section 3.3). The remaining four panels tested in shear with restrained longitudinal deformation (FS3–FS6) failed in a rather brittle manner. A hardening range (ii) was hardly present in FS3 and FS5. These two panels failed shortly after the first crack had formed at very low strains. FS4 and FS6 showed a minor hardening range with some increase of the shear stress after initial cracking. However, the peak load was still reached at very low deformations with $\gamma_{xz,ult} \approx 0.5$‰ for FS4 and $\gamma_{xz,ult} \approx 0.9$‰ for FS6.

The axial compression $-\sigma_x$, in FS3–FS6, which developed due to the longitudinal restraint, followed a very similar path in all tests until reaching the peak load. The same holds for the vertical strain ε_z. As expected, a slight longitudinal expansion of the specimen ($\varepsilon_x > 0$) occurred in the hardening range of FS4 and FS6 due to the longitudinal

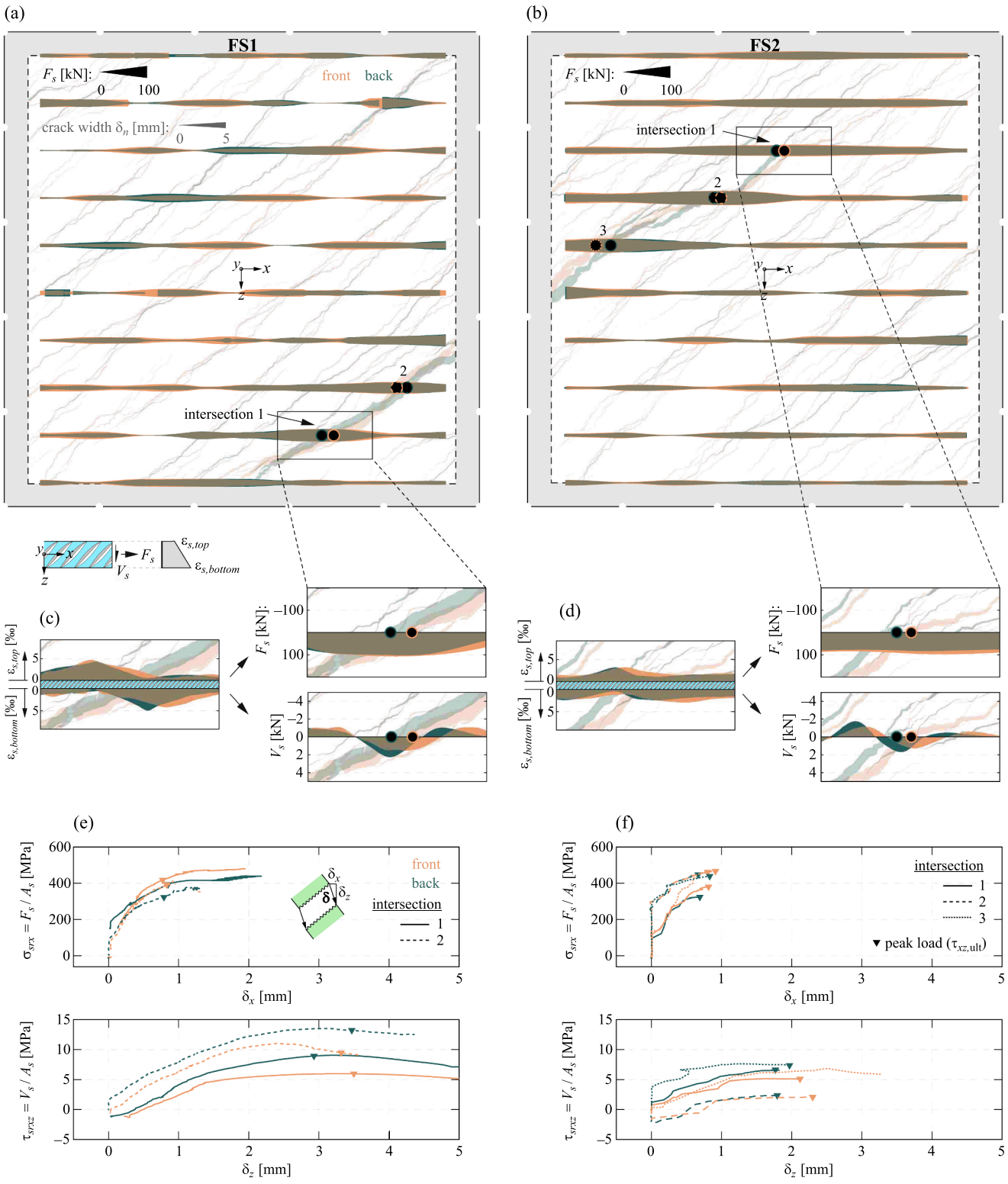

Fig. 13. Behaviour of the longitudinal bar reinforcement of FS1 and FS2 obtained from the DFOS measurements: (a), (b) normal forces of the bars superimposed over the crack patterns from Fig. 11; (c), (d) normal and shear forces of the bars at the crack–bar intersection 1; (e),(f) mean normal and shear stresses versus the corresponding crack kinematic components at the inspected crack–bar intersections. Orange and blue-green circles indicate the location of intersections of front and rear reinforcing bar layers with cracks. (For interpretation of the references to colour in this figure legend, the reader is referred to the web version of this article.)

compliance of the LUSET. The ε_x-path of the two experiments tested in pure shear (FS1 and FS3) was almost identical and reached in both tests $\varepsilon_{x,ult} \approx 1‰$ at the peak load.

The nominal shear strength $\tau_{xz,ult}$ of FS1–FS5 ranged between 2 and 3 MPa and reached $\tau_{xz,ult} = 6.9$ MPa for FS6. In general, higher shear strengths were achieved in experiments with higher fibre contents and in experiments with restrained longitudinal deformation compared to the specimens tested in pure shear. This does not hold for FS5, where a premature failure of the specimen occurred (see Section 3.1). FS3 and FS4, which differ merely in the light longitudinal reinforcement $\rho_{s,x} = 0.28\%$ present only in FS3, had almost identical shear strengths. Other than expected, the bar reinforcement of FS3 thus neither increased the resistance nor the deformation capacity compared to FS4. It is important to note, however, that the strain at the peak load and the subsequent softening behaviour in FS3–FS6 were found to be highly dependent on the crack pattern and the position of the localised crack, as shown in the next section.

3.3. Crack behaviour

Fig. 11 shows the overlaid crack patterns of the front (orange) and back (blue-green) surfaces of the specimens FS1–FS6 at the peak load. The crack patterns and the crack kinematics were obtained with the Automated Crack Detection and Measurement (ACDM) software [31,32] based on the quasi-continuous displacement and strain fields obtained from digital image correlation (DIC) measurements. In the plots, the line thicknesses are proportional to the measured crack widths δ_n. Note that detecting and measuring the extremely closely spaced and fine cracks of the ultra high-performance fibre-reinforced concrete (UHPFRC) in FS6 over the entire specimen surface required a high-quality instrumentation and optimum DIC and ACDM configurations (see Appendix B.2). The cracks on the front and back side match well, which indicates that the cracks formed approximately orthogonally to the panel surface. Crack localisation can be clearly identified in all experiments already at the peak load. Note that due to the premature brittle failure of FS5 at initial cracking, caused by the applied shear force-controlled loading, the crack pattern of this experiment is shown a short instance after reaching the peak load. The crack patterns were significantly influenced by the presence of longitudinal reinforcing bars and the loading type of the specimens. FS1 and FS2, both tested in pure shear, exhibited a crack pattern with multiple cracks at almost uniform spacing induced by the bar reinforcement. The cracks in the other four experiments (FS3–FS6) – all tested in shear with restrained longitudinal deformation and not containing bar reinforcement except for FS3 – were concentrated in relatively small areas. Even though the crack initiator plates triggered cracks at the top and bottom edges of the specimens, no crack pattern with distributed cracks over the entire element formed in these tests. Also, the light longitudinal reinforcement of FS3 was insufficient to induce multiple cracks; the specimen failed shortly after initial cracks had formed in the upper left and lower right corners. For the specimens not exhibiting distributed cracking (FS3–FS5), the crack initiator plates induced diagonal cracks at the corners of the specimens. This resulted in relatively short dominant cracks, making it difficult to control the test. It is therefore recommended to exclude the crack initiator plates in forthcoming tests. FS6, the specimen made from UHPFRC, exhibited a region with many closely spaced and fine cracks, while the remaining specimen was uncracked. FS2 and FS4 failed with a relative rotation of the two faces of the crack in which the deformations localised, as indicated by the cracks opening more on one side.

The crack behaviour of the tests was examined analytically by consolidating the full-field results into equivalent homogeneous cracks, i.e. one set of straight parallel cracks with uniform spacing, opening direction and magnitude. This is a fundamental assumption of the element behaviour in established mechanical models for structural concrete (that have already been extended to include fibre reinforcement, e.g. [4,36–39]). Since the conducted panel tests were homogenous in terms of their geometry, reinforcement and loading, the extraction of the experimental equivalent homogenous cracks – denoted as characteristic cracks (with characteristic values of the crack kinematics, crack inclination and crack spacing) – provides highly valuable information for the development and validation of such models and allows a systematic and comprehensive investigation of the crack behaviour. The determination of the characteristic cracks follows the procedure proposed in [31], where details on their computation are provided in Appendix D. Fig. 12 illustrates the observed characteristic crack kinematic vectors $\boldsymbol{\delta}$ (relative displacement of the two opposite crack faces), crack inclinations θ_r and crack spacings s_r. The crack kinematic vector $\boldsymbol{\delta}$ is defined by its opening and sliding components δ_n and δ_t, respectively, hence the crack opening angle with respect to the crack plane is defined by $\tan(\alpha_r) = \delta_n/\delta_t$. Since the crack opening and sliding are coupled by the crack inclination θ_r, the crack displacement magnitude $\delta = |\boldsymbol{\delta}|$ and its opening direction with respect to the x-axis $\beta_r = 180 - \theta_r - \alpha_r$ are analysed instead.

Initially, the characteristic cracks formed diagonally ($\theta_r = 45°$) and opened orthogonally ($\alpha_r = 90°$) in all experiments. Subsequently, the cracks flattened and started to slide. In FS1 and FS2 the flattening of the cracks corresponded to the successive activation of the longitudinal bar reinforcement. In FS3–FS6, the applied longitudinal compression resulted in a progressive rotation of the principal compressive directions of applied stresses toward the x-axis, leading to gradually flatter cracks. At the peak load, the characteristic cracks of FS1 and FS2 were inclined at $\theta_r \approx 35°$ and opened at $\alpha_r \approx 80°$, which indicates a significant crack sliding component. Similar characteristic crack inclinations and opening angles were observed in FS3–FS6. In the softening range of FS1 the characteristic crack opened almost vertically. Even larger crack sliding was observed in the post-peak range of FS3 and FS4. Almost no change in characteristic crack inclination or crack kinematic opening direction was observed in the softening range of FS6. However, the reliability of the post-peak behaviour of FS4 and FS6 is questionable due to the structural instabilities that occurred in these experiments after reaching the peak load (see Section 3.5). Note that the specimens FS2 and FS5 were loaded shear force-controlled and thus, the post-peak behaviour could not be observed.

While the characteristic crack displacement magnitude δ monotonically increased in all experiments after the onset of cracking, the characteristic crack spacings s_r gradually decreased during the formation of cracks and reached a minimum at the peak load. The subsequent increase of s_r in the softening range of the experiments is related to the crack localisation. The fact that the minimum value of s_r in FS1 and FS2 was reached shortly before the peak load indicates that crack localisation had already started in the hardening ranges of these tests. The behaviour of the characteristic cracks of FS1 and FS2 was almost identical: At the peak load, the characteristic cracks had opened several millimetres, and the well-distributed cracks in both tests resulted in a characteristic crack spacing s_r around 0.5 m. The other four tests, and in particular FS5, exhibited rather brittle failures with significantly higher values of s_r and characteristic crack displacement magnitudes δ less than 1 mm.

3.4. Bar reinforcement behaviour

This section presents the key results from the distributed fibre optical sensing (DFOS) along all longitudinal reinforcing bars in FS1 and FS2 (both loaded in pure shear) and discusses the influence of this distributed bar reinforcement on the structural behaviour of the panels. The DFOS strain measurements at the top and bottom of each bar were transformed into normal forces, bending moments and shear forces of the bars as outlined in Section 2.5. The shear force carried by the reinforcing bars across a crack is known as dowel action.

Fig. 13(a) and (b) show the normal force profiles in the reinforcing bars of FS1 and FS2 at the peak load together with the corresponding

crack patterns from Fig. 11. Of particular interest are the bar responses at their intersections with the cracks, as formulating equilibrium at the cracks yields valuable insight into the mechanical behaviour of structural concrete, particularly in the case of fibre-reinforced concrete [4,36]. Several intersections of the bars with the governing cracks were identified and further investigated (see definition in Fig. 13(a) and (b). The pronounced decrease in bar normal forces further away from the cracks highlights the stress transfer between concrete and reinforcement by bond. The tensile stresses induced by bond to the fibre-reinforced concrete triggered next cracks resulting in a crack pattern with multiple distributed diagonal cracks [4,5,1,36]. Thus, as highlighted by the observed crack patterns in panels with and without longitudinal bar reinforcement (Fig. 11), such a reinforcement has a highly beneficial influence on the crack spacings in fibre-reinforced concrete.

Fig. 13(c) and (d) illustrate the steel strain profiles measured at the top and bottom of the bars ($\varepsilon_{s,top}$ and $\varepsilon_{s,bottom}$) near the bar–crack intersection 1 of FS1 and FS2 and the corresponding normal forces F_s and shear forces (dowel action) V_s, respectively. While F_s varied only slightly in the vicinity of the intersections, V_s changed abruptly. Hence, for the analysis of the dowel action at the crack, the identification of the intersections is highly sensitive to slight misalignments. To minimise the latter, great effort was thus put into measuring accurately the positions of the fibre optical sensors and the coordinates of the DIC data. The intersections were inspected with special care and identified independently at the front and back side of the specimen with the corresponding reinforcement layers (orange and blue-green circles in Fig. 13). It was assumed that the cracks formed orthogonally to the panel surface in the concrete cover, which measured 25 mm on both sides (see Fig. 2). Fig. 13(e) and (f) show the nominal normal and shear stresses (σ_{srx} and τ_{srxz}) acting on the bars (as the average over the cross-section) against the horizontal and vertical components of the crack kinematic vectors (δ_x and δ_z), respectively, at the inspected intersections. σ_{srx} gradually increased with δ_x, following a similar path at all intersections. Note that the peak loads of the panels were reached before the maximum normal stresses in the bars. This could, however, only be observed in FS1, where the softening range of the experiment could be tested. Although the mean normal stresses in the bar did not reach the yield plateau (see also Fig. 4) at the intersections, parts of the bar cross-sections significantly yielded as a result of the superimposed bending acting on the bar. The shear stresses τ_{srxz} increased with δ_z and reached their maximum approximately at the peak loads of the panels. Initial negative τ_{srxz} occurred as a reaction to adjacent cracks that formed before.

Generally, the variation of τ_{srxz} across the intersections was higher than of σ_{srx}, especially for FS2. As a consequence of the normal force–bending moment interaction, larger τ_{srxz} were associated with lower σ_{srx} and vice versa. Nevertheless, the crack kinematics at peak load were almost uniform throughout the intersections. At the peak load, the bar reinforcement contributed significantly to the equilibrium at the crack [4,36,40] by their normal force ($\rho_s\sigma_{srx}$), similar as in conventional reinforced concrete, and was thus essential for the post-cracking shear strength. On the other hand, the contribution of the dowel action ($\rho_s\tau_{srxz}$) to the shear resistance of the panels was only a few percent (on average 4.1% and 1.6% in FS1 and FS2, respectively) and thus indeed negligible as often presumed by mechanical models.

3.5. Stability of the tests during the post-peak range

Four of the six specimens (FS1, FS3, FS4 and FS6) were tested by monotonically increasing the shear strain of the panel in order to observe the post-peak (softening) behaviour as well. While FS1 and FS3 were loaded successfully into the post-peak range of the experiments, undesired deviations from the specified loading paths arose in FS4 and FS6 after reaching the ultimate shear stress.

As already introduced in Section 2.5, the Large Universal Shell Element Tester (LUSET) servo-controlled the best-fit homogeneous plane strain $\boldsymbol{\varepsilon}^*$ of the specimen determined based on the displacement measurements of the actuators. Therefore, the controlled strain $\boldsymbol{\varepsilon}^*$ included the deformations of the LUSET (in the following denoted as $\boldsymbol{\varepsilon}^{(machine)}$) besides the panel deformation $\boldsymbol{\varepsilon}$, i.e. $\boldsymbol{\varepsilon}^* = \boldsymbol{\varepsilon} + \boldsymbol{\varepsilon}^{(machine)}$.

As discussed in detail in Appendix E, FS4 and FS6 could not be controlled in a stable manner due to the relatively low machine stiffness of the LUSET in shear: the release of elastic shear deformation (mainly contained in the machine) during the post-peak range exceeded the shear deformation due to crack localisation, which led to instability after peak load when trying to increase the shear strain that included the machine deformation.

4. Conclusion

Replacing conventional reinforcing bars with fibres can provide considerable economical and ecological benefits, as manual work for assembling and placing the reinforcement is no longer necessary and thinner structures become possible. However, despite the great potential of fibres as shear reinforcement already shown by several experimental studies, the application of fibre-reinforced concrete (FRC) in structural elements is very limited. This is largely due to a lack of understanding of the mechanical behaviour of the fibre-reinforced concrete subjected to shear. Furthermore, hardly any large-scale tests on elements with moderate fibre contents relevant for practice have been conducted to date.

This paper presents an experimental research aiming at closing this knowledge gap. Six fibre-reinforced concrete panels with dimensions of 2.00 m × 2.00 m × 0.27 m representing girder webs were tested in the Large Universal Shell Element Tester (LUSET) of ETH Zurich. Five of these specimens contained moderate fibre dosages between 40 and 60 kg/m^3. Additionally, one specimen made of ultra high-performance fibre-reinforced concrete (UHPFRC) was tested. Four specimens were reinforced solely with fibres (or in one case with very light longitudinal bar reinforcement of $\rho_{s,x} = 0.28$ %) and loaded in shear with restrained longitudinal deformation. The other two specimens contained additional conventional longitudinal reinforcement of $\rho_{s,x} = 0.94$ % and were tested in pure shear. A loading module for the shear strain-controlled testing of the panels was developed and implemented in the LUSET to test the post-peak behaviour in four of the panels.

The crack behaviour of the panels was studied in detail using full-field digital image correlation (DIC) measurements. By applying the Automated Crack Detection and Measurement (ACDM) tool developed by the authors, the complete crack patterns with measurements of the crack kinematics were obtained on both sides of the specimens. The data was consolidated into characteristic cracks allowing a systematic and comprehensive investigation of the crack inclinations, spacings, opening directions and magnitudes. In the two specimens with conventional reinforcement, the crack measurements obtained from ACDM were combined with distributed fibre optical sensing (DFOS) of the reinforcing bars allowing a deeper insight into the structural behaviour of these elements. Based on the experimental results and discussion presented, the following main conclusions are drawn:

- Overall, the test results highlight the high efficiency of the fibres as shear reinforcement in large-scale web elements. An increase of the load after initial cracking (i.e. hardening response) was observed in all experiments with one exception, though all specimens failed by crack localisation.
- The four specimens with no or only little distributed bar reinforcement, which were tested in shear with restrained longitudinal deformation, failed rather brittle with only a few cracks formed over the element. The two experiments with significant longitudinal bar reinforcement distributed over the element height, which were tested in pure shear, showed a significantly increased ductility with multiple well-distributed cracks over the elements. These results indicate that the control of the longitudinal panel deformations by

means of bar reinforcement is highly beneficial to the crack behaviour.

- The UHPFRC panel showed a notable increase in shear strength compared to the other panels made from FRC with moderate amounts of fibres and normal-strength concrete. However, the much higher fibre content was still unable to generate distributed cracks: While many closely spaced and fine cracks formed over a region in this panel, most of the specimen remained uncracked. Thus, the deformation capacity of the UHPFRC panel was highly limited.
- The replacement of conventional minimum shear reinforcement with fibres is only appropriate in cases where distributed cracks are guaranteed. Until further data become available, it is proposed that web elements without conventional minimum shear reinforcement shall contain longitudinal bar reinforcement, uniformly distributed over the web height, with a reinforcement ratio of at least 0.9% in order for the fibres to be considered effective as shear reinforcement.
- Instabilities with undesired deviations from the specified loading path occurred in the post-peak range of two experiments. These instabilities could be attributed to the high compliance of the LUSET in shear. Possible solutions for preventing post-peak instability problems in future shear panel tests were proposed.

CRediT authorship contribution statement

Nicola Gehri: Conceptualization, Methodology, Investigation, Writing – original draft, Visualization, Project administration, Funding acquisition. **Jaime Mata-Falcón:** Conceptualization, Methodology, Validation, Writing – review & editing, Supervision. **Walter Kaufmann:** Conceptualization, Methodology, Writing – review & editing, Funding acquisition.

Declaration of Competing Interest

The authors declare that they have no known competing financial interests or personal relationships that could have appeared to influence the work reported in this paper.

Data availability

The complete experimental data presented in this article is shared in a public data repository accessible on https://doi.org/10.3929/ethz-b-000608583.

Acknowledgements

The authors gratefully acknowledge the financial support of cemsuisse for the project (project number 202007), N.V. Bekaert SA for sponsoring the Dramix® fibres and Holcim AG for sponsoring the Ductal® UHPFRC. They further acknowledge the support of the staff of the Structures Laboratory at ETH Zurich, as well as Fiorentina Ademi, Luca Angst, Davide Ferrari and Tena Galkovski during the preparation and execution of the experiments.

Appendix A:. Characterisation of the fibre-reinforced concrete mixes

This appendix provides details on the fibre-reinforced concrete material characterisation tests conducted in parallel with the panel experiments in the Large Universal Shell Element Tester.

For each fibre-reinforced concrete batch in FS1–FS5, a slump test was conducted immediately before casting. The slump ranged between 41 and 53 cm (see Table A.1), which allowed proper compaction of all panels. In addition, the air void content p_c was determined. Note that FS1/FS3 and FS2/FS5, respectively, were cast together from the same batch, thus showing identical fresh concrete properties. No fresh concrete tests were carried out in FS6, as this concrete was a ready-mix ultra high-performance fibre-reinforced concrete (UHPFRC) that was mixed and cast on-site under the guidance of a product expert from the supplier, who ensured a proper consistency.

The mechanical properties of the hardened fibre-reinforced concrete were determined at the same time as the experiments (with a maximum

Table A1
Properties of the fresh and hardened fibre-reinforced concrete.

Specimen	Slump[cm]	p_c[%]	Cylinder compressive strength f_c: # samples mean (CV) [MPa]	Residual flexural tensile strengths [(1)]: # samples $f_{R,1}$: mean (CV) [MPa] $f_{R,3}$: mean (CV) [MPa]		
				Cut	Formed	All
FS1	53.0	1.25	6 50.3 (0.08)	2 5.7 (0.24) 5.9 (0.27)	3 4.1 (0.19) 4.7 (0.15)	5 4.6 (0.26) 5.1 (0.22)
FS2	48.5	1.7	3 45.8 (0.05)	1 6.6 (–) 5.6 (–)	4 5.6 (0.08) 5.0 (0.14)	5 5.8 (0.10) 5.2 (0.13)
FS3	53.0	1.25	6 49.5 (0.08)	2 4.4 (0.21) 4.9 (0.37)	4 3.7 (0.42) 3.9 (0.36)	6 3.9 (0.34) 4.3 (0.34)
FS4	41.0	1.8	6 46.4 (0.03)	2 3.1 (0.16) 3.5 (0.12)	3 4.3 (0.05) 5.0 (0.09)	5 3.8 (0.19) 4.4 (0.21)
FS5	48.5	1.7	6 48.3 (0.05)	2 5.3 (0.30) 4.9 (0.25)	4 7.7 (0.12) 7.1 (0.20)	6 6.9 (0.19) 6.3 (0.21)
FS6 (UHPFRC)	–	–	6 169.9 (0.10)	2 11.0 (0.15) 9.5 (0.05)	2 21.2 (0.23) 18.2 (0.51)	4 16.1 (0.41) 13.8 (0.53)

[(1)] According to EN 14651 [24] at crack mouth opening displacements $CMOD_1 = 0.5$ mm and $CMOD_3 = 2.5$ mm, respectively; complete $CMOD$–f_R-curves are provided in Fig. A.1.

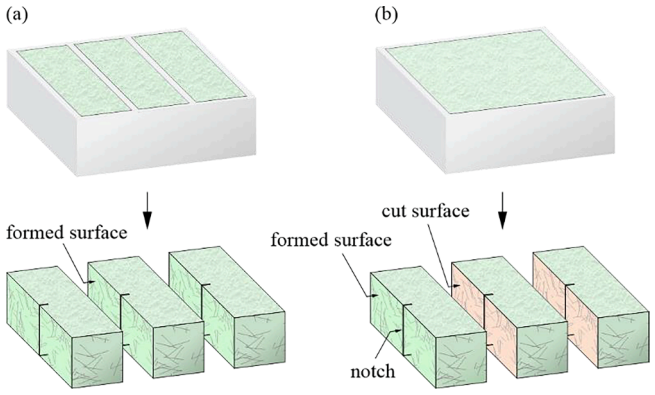

Fig. A1. Production of the notched beams for the companion three-point bending tests: (a) specimens cast in individual moulds; (b) specimens cut from a larger sample.

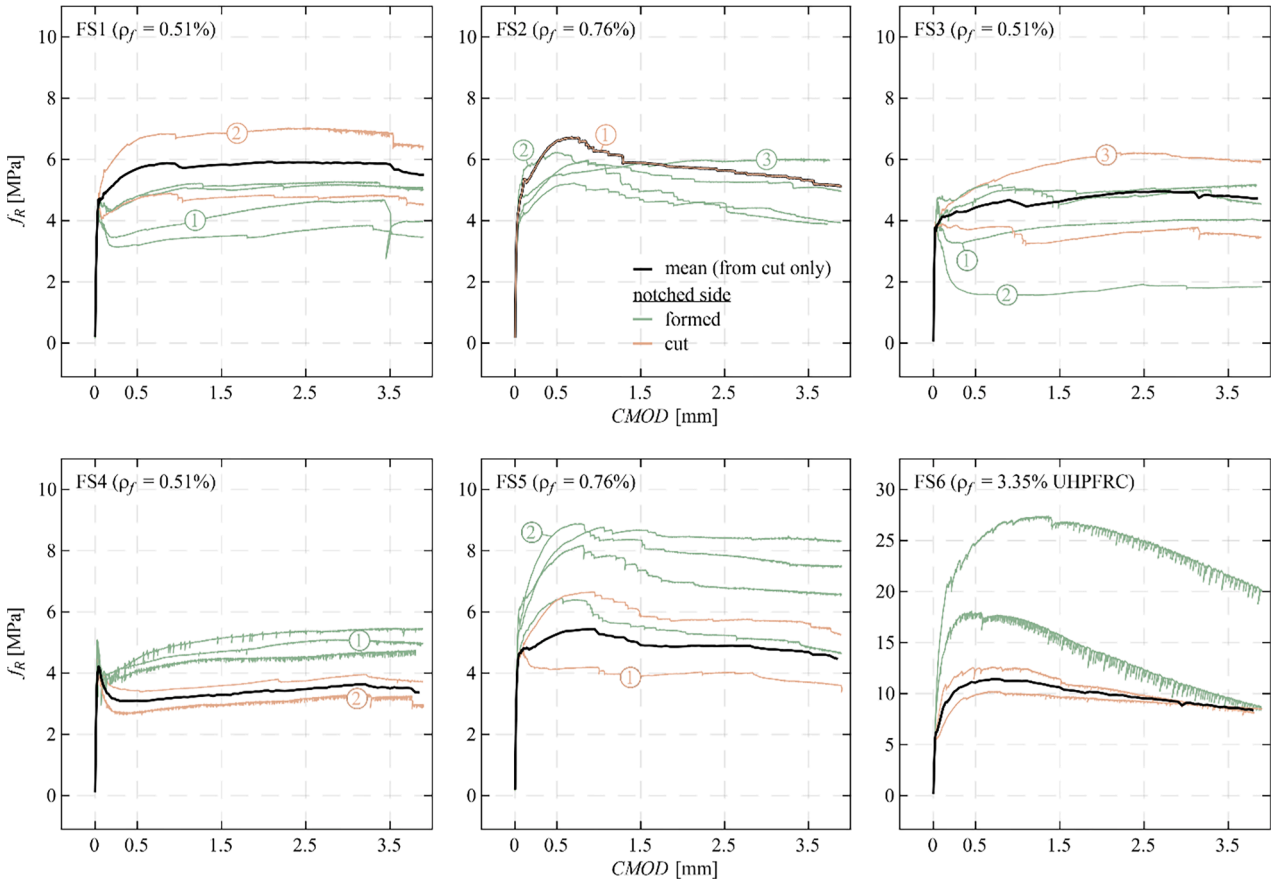

Fig. A2. Results from bending tests on notched beams to characterise the residual flexural tensile strength of fibre-reinforced concrete according to EN 14651 [24] (circled numbers indicate beam no. in Table A.2).

Table A2
Fibre counts in the failure plane of the beams used to characterise the residual flexural tensile strength.

Specimen	Beam no.[1]	Fibre counts in both sections of the failure plane[2] [–] ($\rho_{f,eff,2D}$ | $\rho_{f,eff,3D}$) [%]				
		Section 1	Section 2	Section 3	Section 4	Section 5
FS1	1	19 (0.35 | 0.45)	26 (0.48 | 0.61)	19 (0.35 | 0.45)	18 (0.33 | 0.42)	40 (0.74 | 0.94)
	2	34 (0.63 | 0.80)	41 (0.76 | 0.97)	34 (0.63 | 0.80)	19 (0.35 | 0.45)	27 (0.50 | 0.64)

(*continued on next page*)

Table A2 (*continued*)

Specimen	Beam no.[1]	Fibre counts in both sections of the failure plane[2] [–] ($\rho_{f,eff,2D}$ | $\rho_{f,eff,3D}$) [%]				
		Section 1	Section 2	Section 3	Section 4	Section 5
FS2	1	18 (0.33 | 0.42)	33 (0.61 | 0.78)	29 (0.54 | 0.68)	42 (0.78 | 0.99)	51 (0.94 | 1.20)
	2	38 (0.70 | 0.90)	40 (0.74 | 0.94)	15 (0.28 | 0.35)	33 (0.61 | 0.78)	73 (1.35 | 1.72)
	3	28 (0.52 | 0.66)	29 (0.54 | 0.68)	16 (0.30 | 0.38)	34 (0.63 | 0.80)	59 (1.09 | 1.39)
FS3	1	29 (0.54 | 0.68)	14 (0.26 | 0.33)	34 (0.63 | 0.80)	31 (0.57 | 0.73)	22 (0.41 | 0.52)
	2	12 (0.22 | 0.28)	8 (0.15 | 0.19)	14 (0.26 | 0.33)	18 (0.33 | 0.42)	25 (0.46 | 0.59)
	3	46 (0.85 | 1.08)	20 (0.37 | 0.47)	29 (0.54 | 0.68)	28 (0.52 | 0.66)	35 (0.65 | 0.82)
FS4	1	27 (0.50 | 0.64)	19 (0.35 | 0.45)	30 (0.56 | 0.71)	28 (0.52 | 0.66)	27 (0.50 | 0.64)
	2	18 (0.33 | 0.42)	16 (0.30 | 0.38)	20 (0.37 | 0.47)	21 (0.39 | 0.49)	22 (0.41 | 0.52)
FS5	1	22 (0.41 | 0.52)	28 (0.52 | 0.66)	18 (0.33 | 0.42)	20 (0.37 | 0.47)	29 (0.54 | 0.68)
	2	41 (0.76 | 0.97)	37 (0.68 | 0.87)	43 (0.80 | 1.01)	54 (1.00 | 1.27)	48 (0.89 | 1.13)

[1] Beam no. corresponds to the circled numbers in Fig. A.2.
[2] Fibres were counted in five horizontal sections 1–5 of equal height of 25 mm (covering together the entire failure plane) on both sides of the failure plane:
Section 1 is at the tension side w.r.t. the loading of the beam;
Section 5 is at the compression side w.r.t. the loading of the beam.

difference of one week). To this end, the uniaxial compressive strengths f_c were obtained by compression tests on standard cylinders with a diameter of 150 mm and a height of 300 mm for FS1–FS5, and on cylinders with a diameter of 70 mm and a height of 140 mm according to the guideline SIA 2052 [26] for FS6. The number of tested samples, mean values and coefficients of variation (CV) for f_c are summarised in Table A.1. The mean values of f_c were around 48 MPa for FS1–FS5. The cylinder compressive strength of FS6 was substantially higher at about 170 MPa. The scatter of f_c was relatively low within an experiment with coefficients of variation of 0.10 at most.

In addition to the cylinder compression tests, the residual flexural tensile strengths f_R (see also Table A.1) were determined by bending tests on notched beams according to EN 14651 [24]. Note that three-point bending tests were also carried out for FS6, although four-point bending tests on un-notched beams – which allow for multiple cracking between the loading points – are typically used for the material characterisation in the case of materials with expected hardening behaviour such as UHPFRC.

For each panel experiment, six beams were typically tested; the actual number of specimens varies since the displacement transducer loosened from the specimen in some experiments, such that they had to be disregarded. The beams were tested in three-point bending with a span between the supports of $l = 500$ mm and a centric load F. The loading was displacement controlled by monotonically increasing the crack mouth opening displacements ($CMOD$) measured at the notch with a displacement transducer. All beams had identical dimensions, with a length of 550 mm, a cross-section of $h \times b = 150$ mm $\times$ 150 mm (height and depth) and a notch (5 mm wide and 25 mm deep) cut in the centre of each beam length at the tension side. However, they differed in their production: Half of the beams (3 samples) were cast in separate moulds as specified by EN 14651 (Fig. A.1 (a)), while the other three beams were cast in a wider mould of 550 mm $\times$ 460 mm $\times$ 150 mm and subsequently cut into three beams (Fig. A.1(b)). The latter procedure was chosen to obtain samples that better represent the dispersion and orientation of the fibres in the panel, i.e., minimise boundary effects which are known to affect the fibre dispersion and orientation together with other factors such as the flow of concrete and the vibration during casting [1,2,41–50]. It was assumed that the beam tests with a formed surface at the tension side might overestimate the strength with respect to the average panel behaviour due to boundary effects, and that this effect could be largely mitigated using beam tests with a cut surface at the tension side.

The residual flexural tensile strength f_R was calculated from the point load F measurements using the following formula:

$$f_R = \frac{3Fl}{2bh_{sp}} \tag{A.1}$$

where h_{sp} is the distance between the tip of the notch and the top side of the beam, measuring 125 mm.

The $CMOD$–f_R-curves for FS1–FS6 obtained from the bending tests are shown in Fig. A.1. The colours of the curves indicate whether the surface at the tension side of the respective beam was formed or cut. Table A.1 compiles the number of tested samples, mean values and CV for f_R evaluated at $CMOD_1 = 0.5$ mm and $CMOD_3 = 2.5$ mm, respectively. Additionally, the statistics were obtained within the groups of formed and cut surfaces at the tension side of the beams, respectively, for assessing the boundary effect.

After testing, the number of fibres crossing the failure plane was manually counted to check the dispersion and orientation of the fibres. For FS1–FS5, the fibres were counted in at least two beams each. Manual fibre counting in FS6 was not feasible due to the high density of the fine fibres. The failure planes were divided into five equal horizontal sections with a height of 25 mm and were inspected on both sides. The fibre counting is reported in Table A.2. The fibre counts were transformed into the effective fibre content:

$$\rho_{f,eff} = \frac{N_T d_f^2 \pi}{4 K_f A_T} \tag{A.2}$$

where N_T is the count of fibres, A_T is the corresponding area of the inspected section of the failure plane (125 mm × 150 mm) and K_f is the fibre orientation factor. The values of $\rho_{f,eff}$ reported in Table A.2 account for the theoretical values of K_f according to [1]: $1/2$ corresponding to a 3D fibre distribution and $2/\pi$ representative of a 2D fibre distribution.

The residual strength was found to correlate very well with the measured effective fibre content. Higher residual strengths were observed particularly in beams with higher fibre counts at the two tension-most sections of the failure planes (i.e. sections 1 and 2 in Table A.2). In the tests with normal-strength concrete and moderate amounts of fibres (FS1–FS5), higher residual flexural tensile strengths f_R were achieved in the tests with more fibres (FS2 and FS5) as expected. Substantially higher strengths were obtained in the UHPFRC beams of FS6, with f_R reaching 27 MPa in one test. Furthermore, a distinct flexural hardening range after cracking was identified in FS2, FS5 and FS6.

Generally, higher strengths were obtained in beams with a formed surface at the tension side due to the aforementioned boundary effect. Therefore, exclusively the results from beams with a cut surface at the tension side were assumed to be representative of the panel experiments and hence were considered for evaluating the mean residual flexural tensile strengths f_R shown in Fig. A.1. For the beams with a cut surface at the tension side showing high strengths (e.g. FS1-Beam1 or FS3-Beam3), significantly more fibres than expected were counted. Overall, the scatter of f_R was rather high (with CV exceeding 0.5 in some cases), which can be mainly explained by a non-uniform fibre dispersion as confirmed by the fibre counting (Table A.2). However, the panel behaviour is expected to be less sensitive to non-uniform fibre distributions as the failure surfaces are much larger than in the material characterisation tests.

Appendix B. . Details on instrumentation, test controlling and data processing

B.1. Homogeneous plain strain computation in the LUSET

This section provides details on the computation of the best-fit homogeneous plane strain $\boldsymbol{\varepsilon}^*$ of a panel in the Large Universal Shell Element Tester (LUSET) determined based on the displacement measurements of the twenty jokes of the LUSET (see Sections 2.5 and 2.6). The strain $\boldsymbol{\varepsilon}^*$ was used to control deformations in the LUSET.

In the first step, the best-fit deformation gradient tensor $\boldsymbol{F}$ and translation $\boldsymbol{t}$ is sought:

$$(\boldsymbol{F}, \boldsymbol{t}) = \underset{\boldsymbol{F}\in\mathbb{R}^{2\times2}, \boldsymbol{t}\in\mathbb{R}^2}{\operatorname{argmin}} \sum_{i=1}^{20} \left\| \left(\boldsymbol{F}\boldsymbol{p}_{i,init} + \boldsymbol{t}\right) - \left(\boldsymbol{p}_{i,init} + \boldsymbol{\Delta p}_i\right) \right\|^2 \tag{B.1}$$

where $\boldsymbol{p}_{i,init}$ denotes the in-plane positions of the twenty yokes in the undeformed state and $\boldsymbol{\Delta p}_i$ the corresponding displacement vectors. The solution procedure of Eq. (B.1) can be found in the appendix of [31].

Subsequently, the deformation gradient tensor $\boldsymbol{F}$ is transformed into the (symmetric) right Lagrangian strain tensor $\boldsymbol{E}$:

$$\boldsymbol{E} = \begin{bmatrix} e_{xx} & e_{xz} \\ e_{zx} & e_{zz} \end{bmatrix} = \frac{1}{2}\left(\boldsymbol{F}^T\boldsymbol{F} - \boldsymbol{I}\right) \tag{B.2}$$

By using the elements of $\boldsymbol{E}$, the best-fit homogeneous plane $\boldsymbol{\varepsilon}^*$ is computed as follows:

$$\boldsymbol{\varepsilon}^* = \begin{bmatrix} \varepsilon_x^* & \gamma_{xz}^*/2 \\ \gamma_{xz}^*/2 & \varepsilon_z^* \end{bmatrix} = \begin{bmatrix} \sqrt{1+2e_{xx}} - 1 & \sin^{-1}\left(2e_{xz}/\sqrt{(1+2e_{xx})(1+2e_{zz})}\right)/2 \\ \sin^{-1}\left(2e_{xz}/\sqrt{(1+2e_{xx})(1+2e_{zz})}\right)/2 & \sqrt{1+2e_{zz}} - 1 \end{bmatrix} \tag{B.3}$$

B.2. DIC and ACDM data

The parameters of the two digital image correlation (DIC) systems measuring the full-field deformations of the front and back surface of the specimens are provided in Tables B.1 and B.2. The DIC data were processed with the Automated Crack Detection and Measurement (ACDM) software [31,32] for evaluating in detail the crack pattern and the crack kinematics. Furthermore, the DIC measurements were used to compute the best-fit homogeneous in-plane strain $\boldsymbol{\varepsilon}$ of the panel according to [31]. The optimum DIC and ACDM parameters were set by following the recommendations in [31]. The minimum detectable crack width in all experiments was approximately 0.01 mm at both surfaces. The smallest detectable crack spacing in FS1–FS5 was around the maximum aggregate size (16 mm). For FS6 a great effort was put into a high-quality speckling pattern on the back surface, which (together with the high-resolution cameras and a thorough examination of the optimum DIC and ACDM parameters for this case)

Table B1
DIC and ACDM parameters that remained constant throughout the FS series.

Parameter	Front	Back
DIC		
Resolution [px/mm]	1.53	2.43
Step size *st* [px]	2	2
Filter size *f* [px]	5	5
ACDM		
Inclination window size *iw* [-][(1)]	25	39
d_1 [px] [(2)]	22	22
d_2 [px] [(2)]	11	11

(1) Corresponding to twice the maximum aggregate size of the concrete.
(2) Set to the optimum values according to [31].

Table B2
DIC and ACDM parameters varied throughout the FS series.

Specimen	DIC		ACDM					
	Subset size *ss* [px]		$T_{\varepsilon 1,inf}$ [1/1000]		$T_{\varepsilon 1,sup}$ [1/1000]		T_r [µm]	
	Front	Back	Front	Back	Front	Back	Front	Back
FS1	15	15	1	2	4	8	4.6[(1)]	4.0[(1)]
FS2	15	15	1	3	4	12	4.0[(2)]	3.0[(2)]
FS3	15	15	1	2	4	8	5.6[(1)]	4.6[(1)]
FS4	15	15	1	3	4	12	4.0[(2)]	2.8[(2)]
FS5	15	15	1	3	4	12	3.8[(2)]	2.8[(2)]
FS6	15	9	1.5	3	6	5	6.4[(1)]	5.6[(1)]

(1) Threshold of accepted uncertainty set to $T_r = 2r_{RMS,ZST}$ according to [31].
(2) No ZST was conducted for these tests. The ZDT was used instead: $T_r = 2r_{RMS,ZDT}$.

allowed the detection and measurement of the extremely closely spaced and fine cracks of the ultra high-performance fibre-reinforced concrete (UHPFRC). With this configuration, the smallest detectable crack spacing could thus be reduced to around 5 mm.

Prior to the experiments, a zero-displacement test (ZDT) and a zero-strain test (ZST) according to Mata-Falcón et al. [23] were carried out to assess the DIC uncertainty. The measurements of these tests were used to set the threshold of accepted uncertainty T_r in the crack kinematic measurements according to [31]. Crack kinematic measurements with uncertainties exceeding T_r (e.g. at locations with closely spaced cracks, crack intersections or high morphological curvature of the crack) were substituted by linear interpolation of neighbouring reliable measurements [32].

Appendix C:. Loading histories of panel tests

This appendix presents the loading histories of the six panel tests FS1–FS6. Figs. C.1–C.6 show the in-plane stress and strain states of each panel over time. The top rows illustrate the nominal stresses ($\tau_{xz}, \sigma_x, \sigma_z$) per specimen edge (south, north, bottom, top). The (theoretically) constant differences of σ_z between the top and bottom edges resulted from the self-weight of the specimen.

The out-of-plane shear stresses as well as the bending and twisting moments were successfully controlled to zero throughout all tests and are therefore not shown. The components of the homogenous panel strains are shown for the different measurement systems in the bottom rows of the figures. On the one hand, the strains $\boldsymbol{\varepsilon}^*$, determined based on the actuator strokes and used to control the panel deformation, are reported (black). On the other hand, the panel strains $\boldsymbol{\varepsilon}$, obtained from the two digital image correlation systems at the front and back surface of the specimen are shown

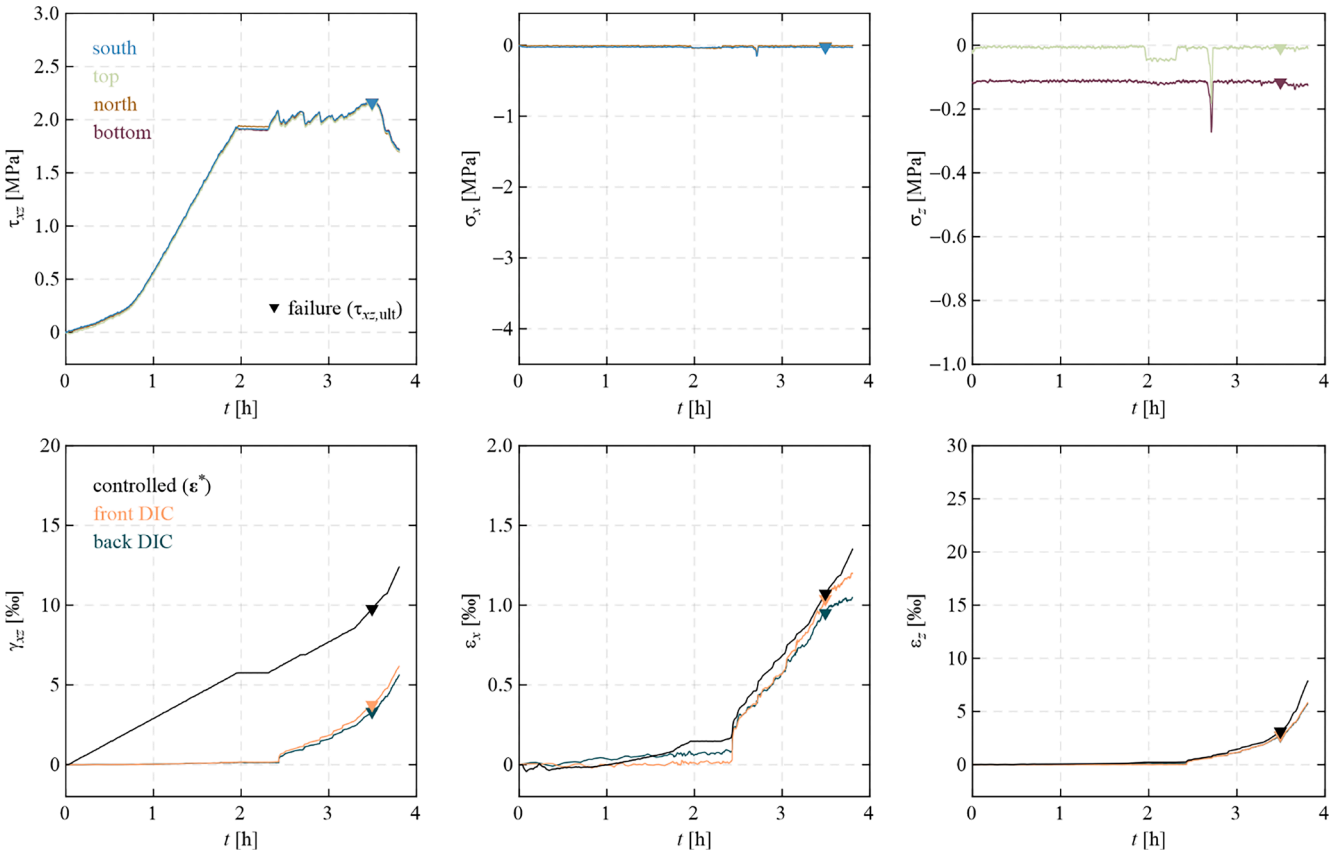

Fig. C1. Loading history of FS1 showing the evolution over time of the in-plane nominal stresses and strains.

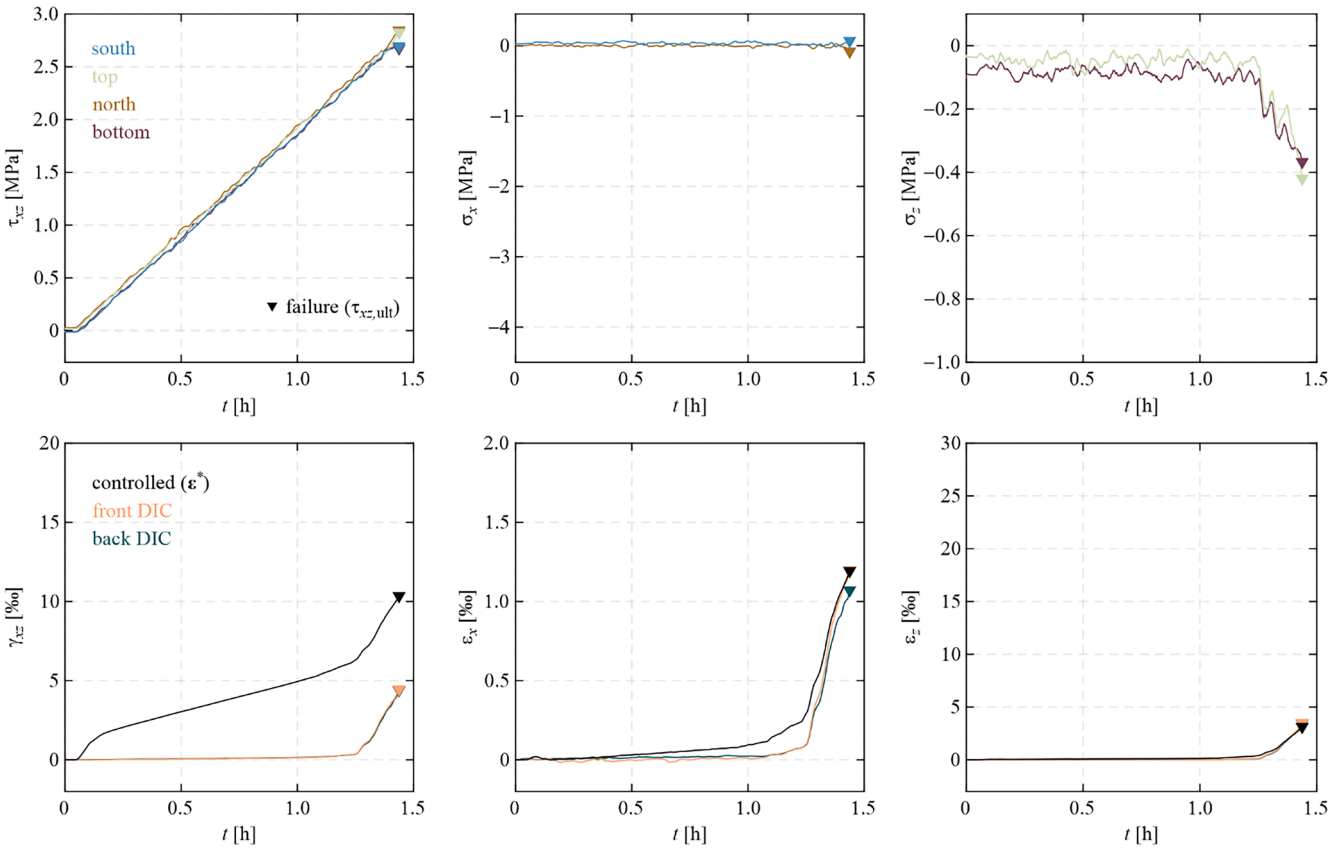

Fig. C2. Loading history of FS2 showing the evolution over time of the in-plane nominal stresses and strains.

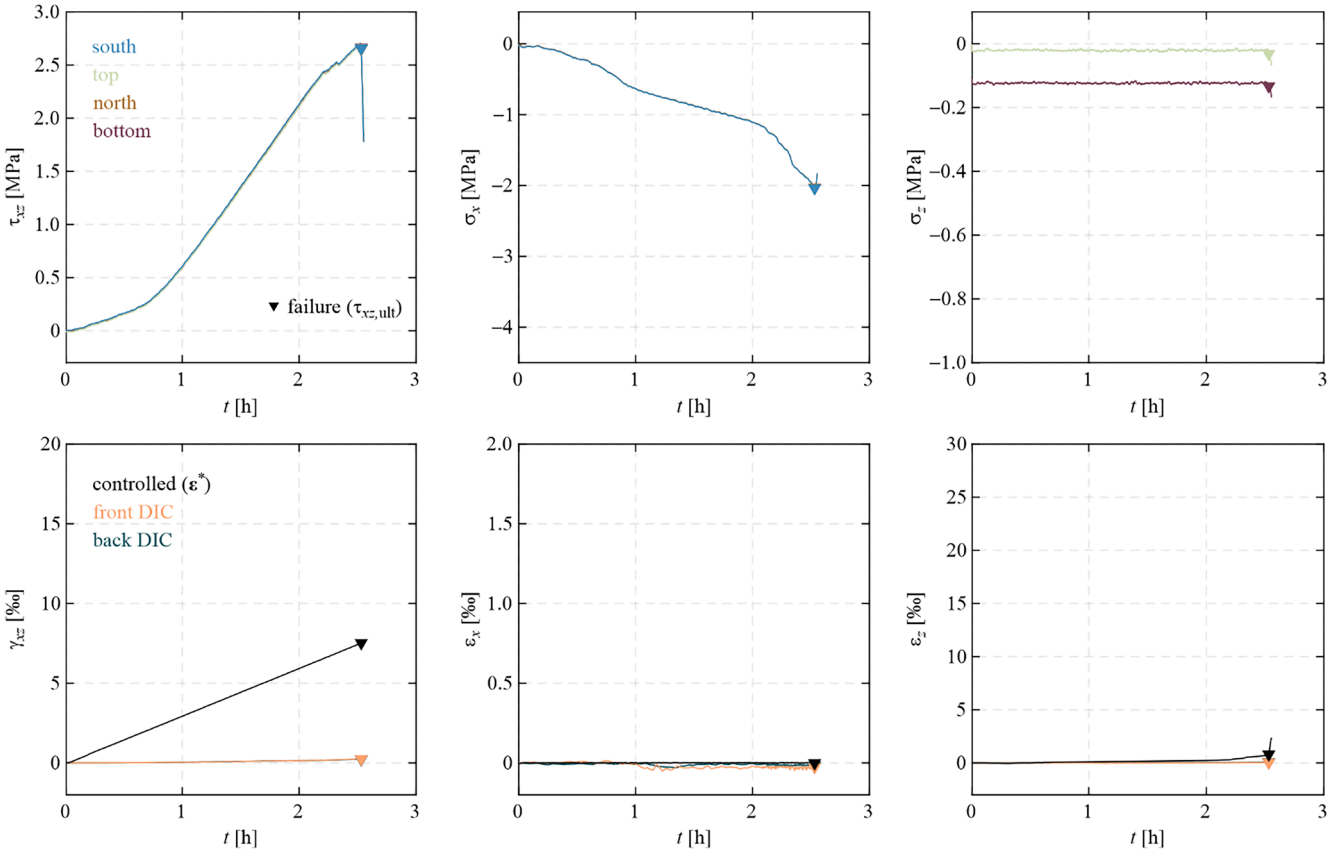

Fig. C3. Loading history of FS3 showing the evolution over time of the in-plane nominal stresses and strains.

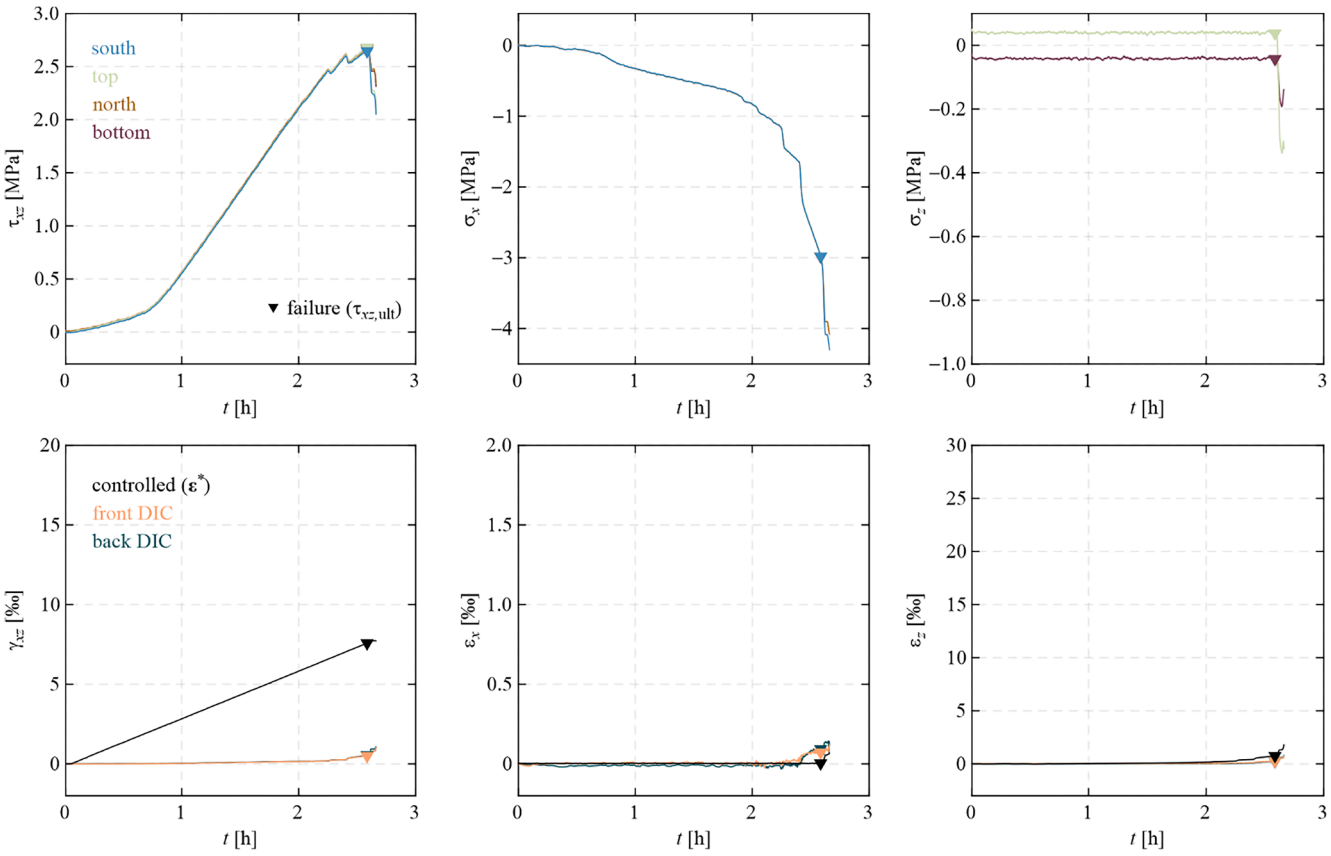

Fig. C4. Loading history of FS4 showing the evolution over time of the in-plane nominal stresses and strains.

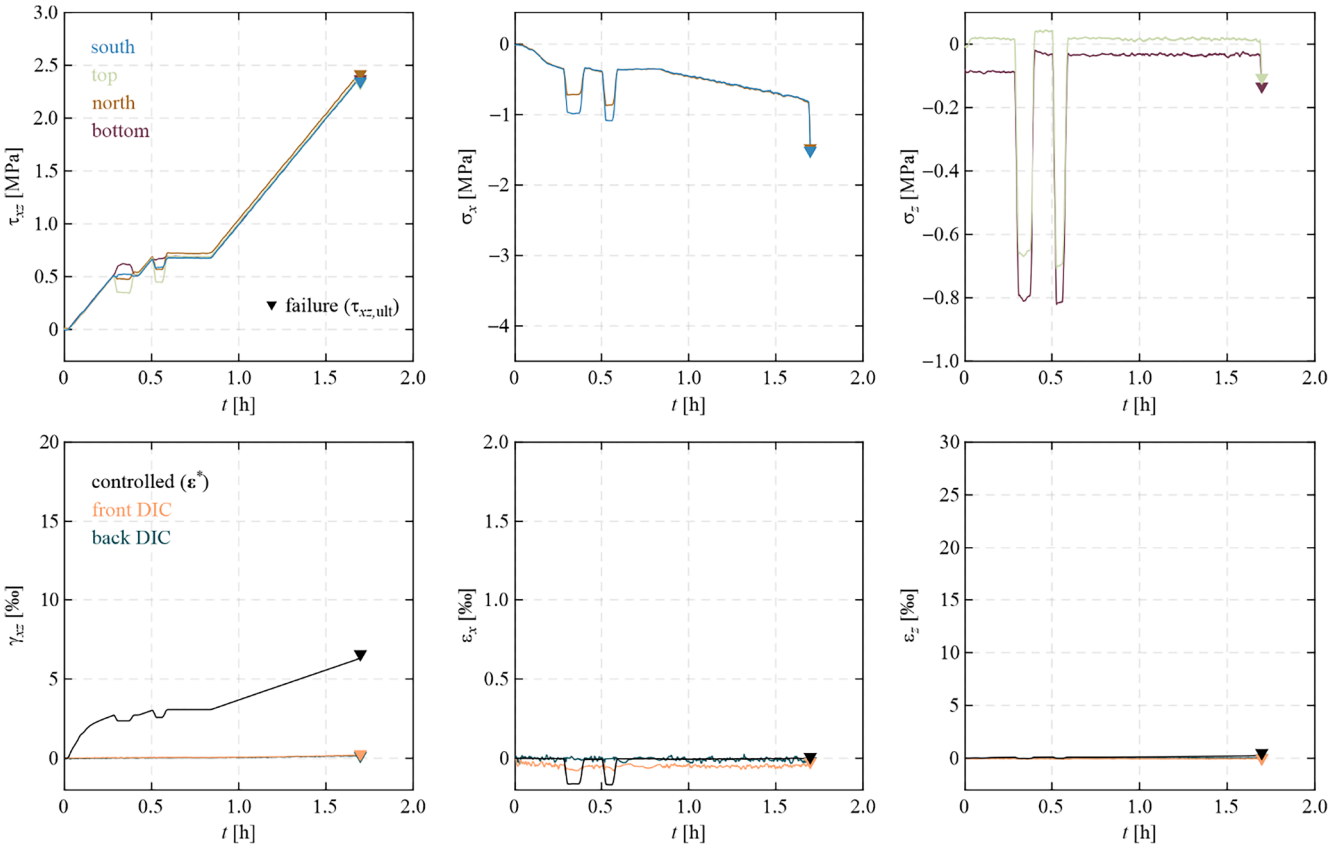

Fig. C5. Loading history of FS5 showing the evolution over time of the in-plane nominal stresses and strains.

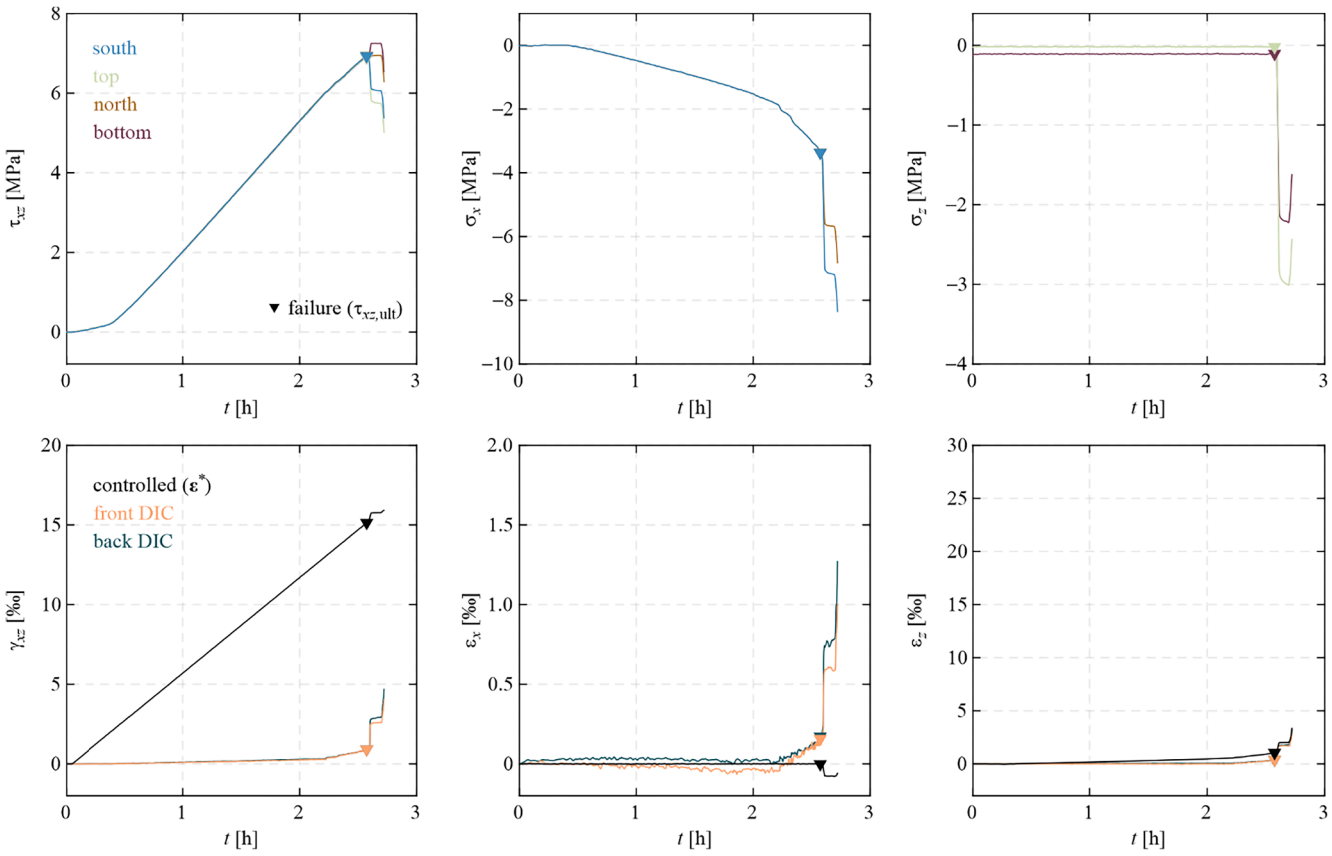

Fig. C6. Loading history of FS6 showing the evolution over time of the in-plane nominal stresses and strains.

(orange and blue-green).

Appendix D:. Derivation of characteristic cracks

This appendix presents the consolidation of the surface deformation from the digital image correlation (DIC) measurements into the equivalent homogeneous cracks discussed in Section 3.3. They represent the characteristic (i) crack displacement magnitude δ (ii) crack opening direction with respect to the x-axis β_r, (iii) crack inclination θ_r, and (iv) crack spacing s_r, which describe the equivalent set of straight parallel cracks with uniform spacing, opening direction and magnitude. The information combines the statistical consolidation of the detailed crack information obtained with the Automated Crack Detection and Measurement (ACDM) software and the direct extraction of the best-fit homogeneous cracks from the DIC displacement measurements. Both approaches were presented in [31] and their results are shown in Fig. D.1 exemplarily for FS1 and FS6. The latter

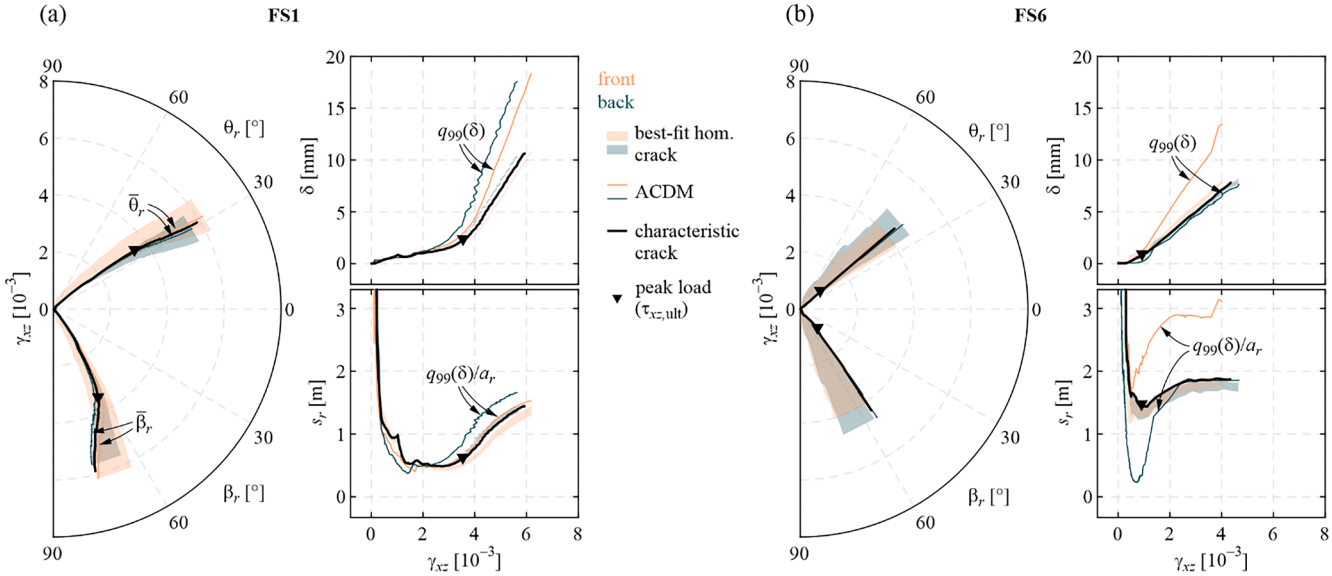

Fig. D1. Crack statistics with statistical consolidation of ACDM and best-fit homogeneous crack for FS1 and FS6.

experiment was chosen to investigate the influence of different DIC and ACDM parameters (see Appendix B.2). While the characteristic crack properties obtained from the ACDM data depend on the chosen statistical parameter (quantile, mean, etc.), the best-fit homogeneous crack approach specifies a range of plausible results bounded by two extreme assumptions about the source of potential principal compressive strains, which are attributed entirely to either (i) concrete deformations between the cracks (i.e., assuming that the cracks open orthogonally) or (ii) skew crack openings (i.e., assuming that the concrete between the cracks is rigid).

As shown in [31], the statistical consolidation of the ACDM results provides highly reliable results for θ_r and β_r by taking the respective mean angles weighted by δ. As shown in Fig. D.1, they were indeed perfectly in the range of plausible results from the best-fit homogeneous crack approach and very similar at the front and back side. Thus, the characteristic crack inclination θ_r and crack kinematic opening direction β_r presented in Section 3.3 were set to the weighted mean angles of the ACDM results.

Since the true crack displacement magnitude and crack spacing within an experiment varied drastically over the tested panels due to crack localisation, the determination of the characteristic values of s_r and δ using the ACDM results would heavily depend on the chosen statistical parameter. Furthermore, as shown in Fig. D.1, the quantiles for FS6 were significantly different at the front and back surface, indicating its strong dependency on the DIC and ACDM parameters. On the other hand, the best-fit homogeneous crack approach resulted in very similar values at the front and back side, with very narrow plausible ranges for s_r and δ. Thus, the characteristic values of these two crack properties shown in Section 3.3 were set to the ones obtained with the mean best-fit homogenous crack between the front and back side, assuming that the compressive strains were due to the concrete deformation. However, note that the two assumptions yielded almost identical results.

Appendix E:. Post-peak stability analysis of panel tests

As introduced in Section 2.5, the Large Universal Shell Element Tester (LUSET) servo-controlled the best-fit homogeneous plane strain $\boldsymbol{\varepsilon}^*$ of the specimen determined based on the displacement measurements of the actuators. Therefore, the controlled strain $\boldsymbol{\varepsilon}^*$ included the deformations of the LUSET (in the following denoted as $\boldsymbol{\varepsilon}^{(machine)}$) besides the panel deformation $\boldsymbol{\varepsilon}$, i.e.

$$\boldsymbol{\varepsilon}^* = \boldsymbol{\varepsilon} + \boldsymbol{\varepsilon}^{(machine)} \tag{E.1}$$

The importance of the machine deformations is apparent in Figs. C.1–C.6 by comparing the panel strains determined from the digital image correlation (DIC) measurements and the controlled strains. While the longitudinal and vertical deformations of the LUSET ($\varepsilon_x^{(machine)}$ and $\varepsilon_z^{(machine)}$) were relatively low, the shear deformation of the LUSET $\gamma_{xz}^{(machine)}$ was significant. As a reference, in the uncracked range of the experiments the increase of the machine deformation $\gamma_{xz}^{(machine)}$ was approximately 25 times higher than that of the panel shear deformation γ_{xz}.

Controlling the tests by increasing the shear strains seemed to be appropriate when designing the test setup, since this deformation component characterises the shear response of panel elements and reacts most sensitively to changes in the shear stress, especially at crack localisation. The latter is an important property of a control variable [51,52]. However, if the testing machine is not stiff enough, the release of elastic shear deformation (mainly contained in the machine) during the post-peak range might exceed the shear deformation due to crack localisation. This would lead to instability after peak load when trying to increase a shear strain that includes the machine deformation (the testing machine is often referred to as non-compliant in such cases [53,54]). This was the case in the experiments FS4 and FS6. Since these instabilities are rather complex in shear tests because the element loading is two-dimensional, the simplified equivalent one-dimensional problem is discussed first in the following.

The post-peak instabilities in tests on linear elements, such as uniaxial compression, tension or bending tests are well studied in the literature (e.g. [51–53,55–57]). The most simple equivalent one-dimensional problem is a linear elastic concrete tie (Elastic modulus E, cross-sectional area A, length l) exhibiting linear softening with the crack opening δ (softening modulus D) loaded in axial tension σ_x in a linearly elastic testing machine with elastic stiffness k (see Fig. E.1(a)). The load is applied by monotonically increasing the controlled strain ε_x^* of the tie that includes the deformations of the machine. Once cracking occurs in the weakest region, the peak load f is reached and crack localisation occurs. The deformations of the tie in the post-peak response can be decomposed into the elastic unloading part of the uncracked concrete and the softening in the localised crack, denoted with the superscripts c and r, respectively. Hence, the post-peak average strains of the tie are

$$\varepsilon_x = \varepsilon_x^{(c)} + \varepsilon_x^{(r)} \tag{E.2}$$

where

$$\begin{aligned} \varepsilon_x^{(c)} &= \sigma_x / E \\ \varepsilon_x^{(r)} &= (f - \sigma_x)/(Dl) \end{aligned} \tag{E.3}$$

The displacements of the testing machine u are proportional to the load $F = \sigma_x A$, i.e, $u = F/k$. Transforming u into the component of controlled strains due to the machine deformation, one gets

$$\varepsilon_x^{(machine)} = \sigma_x A/(kl) \tag{E.4}$$

Combining Eqs. (E.1)–(E.4) results in the controlled strain

$$\begin{aligned} \varepsilon_x^* &= \varepsilon_x^{(c)} + \varepsilon_x^{(r)} + \varepsilon_x^{(machine)} \\ \varepsilon_x^* &= \sigma_x \left(\frac{1}{E} + \frac{A}{kl} - \frac{1}{Dl} \right) + \frac{f}{Dl} \end{aligned} \tag{E.5}$$

Hence, to ensure stable control in the post-peak range (increasing ε_x^* at decreasing σ_x, i.e. $\partial \varepsilon_x^* / \partial \sigma_x < 0$), the following condition needs to be met [57]:

$$\mathrm{X} = \frac{Dl}{E^*} < 1 \tag{E.6}$$

where $E^* = \left(\frac{1}{E} + \frac{A}{kl}\right)^{-1}$ and X is the instability factor.

The post-peak stability of panel tests in the LUSET can be assessed analogously. Fig. E.1(b) shows the simplified test setup and loading with linearised constitutive relationships of the testing machine (elastic stiffness k) and the specimen (shear modulus G). A concrete panel of size $l \times l$ is installed in a panel tester and loaded in pure shear τ_{xz}. The load is applied by monotonically increasing the controlled shear strain γ_{xz}^{*} (component of controlled strain $\boldsymbol{\varepsilon}^{*}$: best-fit homogeneous panel strain based on the measured actuator strokes). Note that it is assumed that the longitudinal compression in FS3, FS4 and FS6 did not affect the post-peak shear behaviour of the panels, such that it can be neglected in the assessment of the post-peak stability. After reaching the peak load f, the deformations localise in an inclined, straight crack, which is assumed to open uniformly with the crack kinematic vector $\boldsymbol{\delta}$ and exhibit a linearly softening shear resistance as a function of the crack face displacement $\delta = |\boldsymbol{\delta}|$ with the softening modulus D. In contrast to the one-dimensional tension tie, the location, inclination and the opening direction of the localising crack, as well as how the best-fit strain is defined, influence the resulting post-peak shear strains in the panel. This effect is accounted for with a geometrical factor η, characterising the influence of the localising crack on the panel shear strain. It is the corresponding best-fit homogeneous shear strain for the given location, inclination and opening direction of a localising crack of unit crack displacement magnitude, multiplied by the panel edge length, i.e. $\eta = \gamma_{xz,\delta=1} l$. Hence, the panel shear strain due to the localised crack can be expressed as $\gamma_{xz}^{(r)} = (f - \tau_{xz})\eta/(Dl)$.

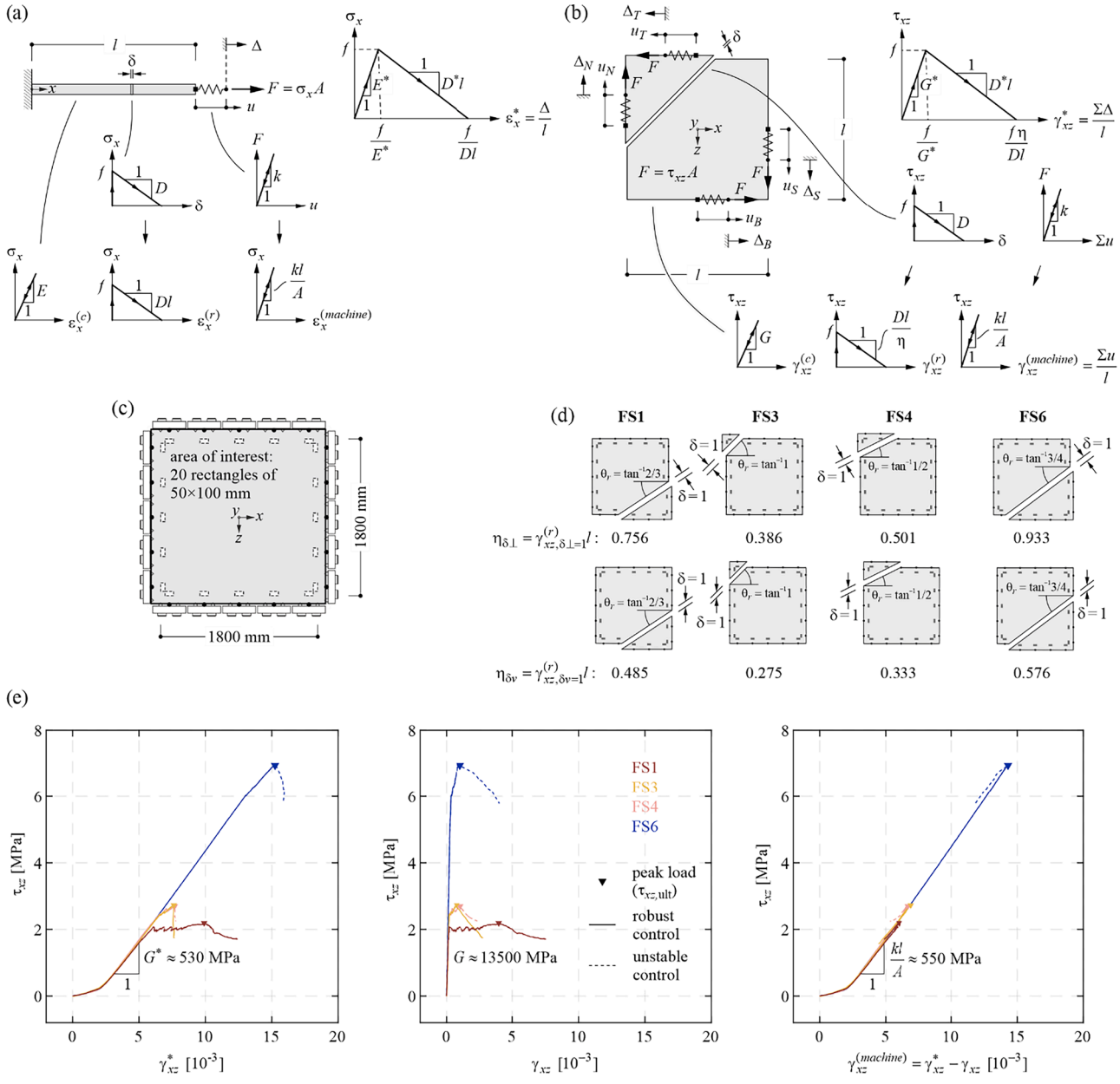

Fig. E1. Post-peak instability estimation of deformation-controlled panel experiments in the LUSET: (a) deformation-controlled testing of a concrete tension tie; (b) deformation-controlled testing of shear panels in a panel tester; (c) determination of the panel strain $\boldsymbol{\varepsilon}$ for the post-peak instability estimation; (d) geometrical factors η describing the influence of the location, inclination, and opening direction of the crack localisation; (e) shear stress responses of FS1, FS3, FS4 and FS6 as a function of the controlled shear strain γ_{xz}^{*}, the panel shear strain γ_{xz} and the shear strain of the machine $\gamma_{xz}^{(machine)}$, respectively.

Table E1
Post-peak stability estimation of shear deformation-controlled panel experiments.

Specimen	$f = \tau_{xz,max}$ [MPa]	l_f [mm]	$D_{est} = 2f/l_f$ [MPa/mm]	$(\eta_{\delta\perp}, \eta_{\delta v})$[-][(1)]	X[-][(2)](stable if X < 1,unstable if X > 1)
FS1	2.17	60	0.072	(0.756, 0.485)	0.35–0.55
FS3	2.71	60	0.090	(0.386, 0.275)	0.86–1.21
FS4[(3)]	2.68	60	0.089	(0.501, 0.333)	0.66–0.99
FS6	6.93	20	0.693	(0.933, 0.576)	2.75–4.46

(1) According to Fig. E.1(d).
(2) Calculated according to Eq. (7) with $G^* = 530$ MPa(extrapolated from Fig. E.1(e)), $D = D_{est}$, $l = 2.0$ m and $\eta = \eta_{\delta\perp}$ and $\eta = \eta_{\delta v}$, respectively.
(3) Instability occurred due to relative rotation of the two crack faces of the crack localisation.

Generalising Eq. (E.6) with the geometrical factor η, the instability factor of a panel test is:

$$X = \frac{Dl}{\eta G^*} \tag{E.7}$$

with $G^* = \left(\frac{1}{G} + \frac{A}{kl}\right)^{-1}$ and $A = lt$, where l is the panel edge length and t the panel thickness.

Fig. E.1(e) shows the nominal shear stresses τ_{xz} of FS1, FS3, FS4 and FS6 versus the controlled shear strain γ^*_{xz}, the panel strains γ_{xz} and the component of controlled strains due to the machine deformation $\gamma^{(machine)}_{xz}$, respectively. Note that here the panel strains $\boldsymbol{\varepsilon}$ were obtained from the DIC measurements on 20 small areas located at the specimen edge close to the yokes (see Fig. E.1(c)) to ensure consistency within the definitions of $\boldsymbol{\varepsilon}^*$, $\boldsymbol{\varepsilon}$ and $\boldsymbol{\varepsilon}^{(machine)}$ (see also Section 2.5). Thus, the values for γ_{xz} in Fig. E.1(e) slightly differ (especially in the post-peak ranges) from the previous results in this paper but allow assessing the machine stiffness more accurately and highlighting the linear elastic unloading of the LUSET. As shown in Fig. E.1 (e), the stiffness of the LUSET was approximately 25 times lower compared to the uncracked specimens. Consequently, most of the controlled strain γ^*_{xz} was generated by elastic energy stored in the machine and released after the peak load had been reached. Instability of the test occurred depending on the softening modulus D and the geometrical factor η.

In Fig. E.1(d), η is derived based on the location and inclination of the experimentally observed localising cracks for orthogonal crack opening ($\delta_\perp$) and vertical crack kinematic opening directions (δ_v). These two directions bound the possible crack displacement directions in panel elements that were longitudinally stiffened (either by distributed bar reinforcement or longitudinal axial compression), which allows the estimation of the instability factor range shown in Table E.1. The softening modulus D is estimated by considering (i) a linear softening of the fibre-reinforced concrete from $(\delta, \tau_{xz}) = (0, f)$ to $(\delta, \tau_{xz}) = (l_f/2, 0)$, where l_f is the fibre length, and (ii) the shear stiffness of the LUSET measured in the experiments (see Fig. E.1(e). Note that the post-peak behaviour is independent of a potential hardening range as long as the panel unloads linearly with G.

The estimated range for the instability factor determined from Eq. (E.7) indicates post-peak stability for FS1 and clear post-peak instability for FS6. This is in good accordance with the experimental observations. The estimated post-peak stability of FS3 and FS4 is ambiguous. Both experiments exhibited rather brittle failures with a pronounced drop in the shear force after reaching the peak load (see Appendix C). However, large deviations from the specified loading paths were only observed in FS4, indicating stable control in FS3. The softening modulus D assumed in FS3 might have been overestimated because the beneficial contribution of the bar reinforcement was neglected. This would result in an effective instability factor lower than the estimation in Table E.1, thus predicting a stable behaviour.

Accordingly, the most critical factor causing post-peak instabilities in panel tests in the LUSET is the low machine stiffness in shear. Theoretically, post-peak instabilities could thus be avoided in future experiments by (i) controlling the tests using direct deformation measurements on the specimen, such as e.g. optical tracking systems or (ii) correcting the existing control system for the machine stiffness. However, with these two solutions, the response of the LUSET would have to be rapid enough to almost instantly release the elastic energy stored in the system when instability is sensed [52]. While the LUSET is equipped with fast servo-valves and high-pressure/high-flow hydraulic supply, it would probably be too slow (even without the currently imposed safety limits on the actuator velocities) to prevent a dynamic failure. Alternatively, the experimental setup could be altered by (iii) testing thinner elements with a reduced stiffness relative to the machine (which might, however, cause buckling problems in very thin elements as potentially required e.g. when testing UHPFRC panels) or (iv) rotating the testing direction by 45° with respect to the x-y coordinate system of the LUSET, similar to the standard test setup in the Shell Element Tester (SET) at the University of Toronto [58,59]. For pure shear loading, the latter would correspond to applying principal tensile and compressive stresses of equal magnitude horizontally and vertically, respectively, such that the shear strain of the panel could be controlled via the horizontal and vertical strain components in whose direction the LUSET is much stiffer. In this way, the post-peak behaviour of shear panels has already been successfully tested in the SET [60]. However, this test setup has the disadvantage that the bar reinforcement needs to be placed at 45° to the edges of the panels and more importantly, restraining the longitudinal deformation of the panels (as in FS3–FS6) would be highly complex. Thus, the most promising solution is deemed to be (v) stiffening the LUSET by means of diagonals, which, however, would make it difficult to retain the digital image correlation (DIC) instrumentation of the specimen that is essential to capture their behaviour of the panels in detail.

References

[1] Pfyl T. Tragverhalten von Stahlfaserbeton. Doctoral Thesis. ETH Zurich, 2003. https://doi.org/10.3929/ethz-a-004502831.
[2] Amin A. Post Cracking Behaviour of Steel Fibre Reinforced Concrete: From Material to Structure. Doctoral dissertation. School of Civil and Environmental Engineering, The University of New South Wales, 2015.
[3] Gebhard L, Mata-Falcón J, Anton A, Burger J, Lloret-Fritschi E, Reiter L, et al. Aligned Interlayer Fibre Reinforcement and Post-tensioning as a Reinforcement Strategy for Digital Fabrication. In: Bos FP, Lucas SS, Wolfs RJM, Salet TAM, editors. Second RILEM International Conference on Concrete and Digital Fabrication. Cham: Springer International Publishing; 2020. p. 622–31. https://doi.org/10.1007/978-3-030-49916-7_63.
[4] Kaufmann W, Mata-Falcón J, Amin A. Compression Field Analysis of Fiber-Reinforced Concrete Based on the Cracked Membrane Model. SJ 2019;116:213–24. https://doi.org/10.14359/51716763.
[5] Marti P, Alvarez M, Kaufmann W, Sigrist V. Tension Chord Model for Structural Concrete. Struct Eng Int 1998;8:287–98. https://doi.org/10.2749/101686698780488875.
[6] Marti P, Alvarez M. Versuche zum Verbundverhalten von Bewehrungsstahl bei plastischen Verformungen. Zürich: Institut für Baustatik und Konstruktion, ETH Zürich; 1996.
[7] Kaufmann W, Amin A, Beck A, Lee M. Shear transfer across cracks in steel fibre reinforced concrete. Engineering Structures 2019;186:508–24. https://doi.org/10.1016/j.engstruct.2019.02.027.

[8] Li VC, Ward R, Hmaza AM. Steel and Synthetic Fibers as Shear Reinforcement. MJ 1992;89:499–508. https://doi.org/10.14359/1822.
[9] Adebar P, Mindess S, St.-Pierre D, Olund B. Shear Tests of Fiber Concrete Beams without Stirrups. Structural Journal 1997;94:68–76. https://doi.org/10.14359/462.
[10] Kwak Y-K, Eberhard MO, Kim W-S, Kim J. Shear Strength of Steel Fiber-Reinforced Concrete Beams without Stirrups. SJ 2002;99:530–8. https://doi.org/10.14359/12122.
[11] Voo YL, Foster SJ, Gilbert RI. Shear Strength of Fiber Reinforced Reactive Powder Concrete Prestressed Girders without Stirrups. ACT 2006;4:123–32. https://doi.org/10.3151/jact.4.123.
[12] Parra-Montesinos GJ. Shear Strength of Beams with Deformed Steel Fibers: evaluating an alternative to minimum transverse reinforcement. Concr Int 2006;28:57–67.
[13] Minelli F. Plain and fiber reinforced concrete beams under shear loading: structural behavior and design aspects. Department of Civil Engineering, University of Brescia; 2005. Doctoral dissertation.
[14] SIA 262. Concrete Structures 2013.
[15] Beck A. Paradigms of shear in structural concrete: Theoretical and experimental investigation. Doctoral Thesis. ETH Zurich, 2021. https://doi.org/10.3929/ethz-b-000482684.
[16] Kaufmann W, Mata-Falcón J, Beck A. Future directions for research on shear in structural concrete. fib Bulletin 85: Towards a rational understanding of shear in beams and slabs, 2018. https://doi.org/10.35789/fib.BULL.0085.Ch20.
[17] Carnovale D, Vecchio FJ. Effect of Fiber Material and Loading History on Shear Behavior of Fiber-Reinforced Concrete. SJ 2014;111:1235–44. https://doi.org/10.14359/51687030.
[18] Chasioti SG, Vecchio FJ. Shear Behavior and Crack Control Characteristics of Hybrid Steel Fiber-Reinforced Concrete Panels. SJ 2017;114:209–20. https://doi.org/10.14359/51689164.
[19] Luo JW, Vecchio FJ. Behavior of Steel Fiber-Reinforced Concrete under Reversed Cyclic Shear. SJ 2016;113:75–83. https://doi.org/10.14359/51687940.
[20] Susetyo J. Fibre Reinforcement for Shrinkage Crack Control in Prestressed. Thesis: Precast Segmental Bridges; 2010.
[21] Kaufmann W, Beck A, Karagiannis D, Werne D. The Large Universal Shell Element Tester LUSET. Zurich: Institute of Structural Engineering, ETH Zurich; 2019.
[22] Kaufmann W, Beck A, Karagiannis D, Werne D. Design, Construction and Capabilities of the Large Universal Shell Element Tester. Hormigón y Acero 2022;73:83–8. https://doi.org/10.33586/hya.2020.2844.
[23] Mata-Falcón J, Haefliger S, Lee M, Galkovski T, Gehri N. Combined application of distributed fibre optical and digital image correlation measurements to structural concrete experiments. Eng Struct 2019.
[24] EN 14651 Test Method for Metallic Fibre Concrete—Measuring the Flexural Tensile Strength (Limit of Proportionality (LOP), Residual). Brussels: European Committee for Standardization (CEN); 2005.
[25] NV Bekaert SA. Product Data Sheet for Dramix 3D 80/60 BG n.d.
[26] SIA. Swiss technical bulletin SIA 2052: Ultra-high performance fiber reinforced concrete (UHPFRC) - Materials, design and execution 2016.
[27] Haefliger S, Fomasi S, Kaufmann W. Influence of quasi-static strain rate on the stress-strain characteristics of modern reinforcing bars. ConBuildMat 2021;287:7. https://doi.org/10.1016/j.conbuildmat.2021.122967.
[28] Haefliger S, Kaufmann W. Influence of cross section loss on the stress-strain characteristics of corroded quenched and self-tempered reinforcing bars. ConBuildMat 2021;282:12. https://doi.org/10.1016/j.conbuildmat.2021.122598.
[29] Haefliger S, Kaufmann W, Thoma K. Modelling the load-deformation behaviour of lap splices with the Tension Chord Model. Eng Struct 2022;252:113606. https://doi.org/10.1016/j.engstruct.2021.113606.
[30] Correlated Solutions. Vic-3D Software Manual 2019.
[31] Gehri N, Mata-Falcón J, Kaufmann W. Refined extraction of crack characteristics in Large-scale concrete experiments based on digital image correlation. Eng Struct 2022;251:113486. https://doi.org/10.1016/j.engstruct.2021.113486.
[32] Gehri N, Mata-Falcón J, Kaufmann W. Automated crack detection and measurement based on digital image correlation. Constr Build Mater 2020;256:119383. https://doi.org/10.1016/j.conbuildmat.2020.119383.
[33] LUNA ODiSI 6000 Data Sheet, 2021.
[34] Galkovski T, Lemcherreq Y, Mata-Falcón J, Kaufmann W. Fundamental Studies on the Use of Distributed Fibre Optical Sensing on Concrete and Reinforcing Bars. Sensors 2021;21:7643. https://doi.org/10.3390/s21227643.
[35] Lemcherreq Y, Galkovski T, Mata-Falcón J, Kaufmann W. Application of Distributed Fibre Optical Sensing in Reinforced Concrete Elements Subjected to Monotonic and Cyclic Loading. Sensors 2022;22:2023. https://doi.org/10.3390/s22052023.
[36] Kaufmann W. Strength and Deformations of Structural Concrete Subjected to In-Plane Shear and Normal Forces. Doctoral dissertation Institut für Baustatik und Konstruktion, ETH Zürich 1998. https://doi.org/10.1007/978-3-0348-7612-4.
[37] Vecchio FJ, Collins MP. The Modified Compression Field Theory for Reinforced Concrete Elements Subjected to Shear. ACI J 1986;83:219–31.
[38] Vecchio FJ. Disturbed Stress Field Model for Reinforced Concrete: Formulation. J Struct Eng ASCE 2000;126:1070–7. https://doi.org/10.1061/(ASCE)0733-9445(2000)126:9(1070).
[39] Minelli F, Vecchio FJ. Compression Field Modeling of Fiber-Reinforced Concrete Members Under Shear Loading. SJ 2006;103:244–52. https://doi.org/10.14359/15182.
[40] Kaufmann W, Marti P. Structural Concrete: Cracked Membrane Model. J Struct Eng 1998;124:1467–75. https://doi.org/10.1061/(ASCE)0733-9445(1998)124:12(1467).
[41] Romualdi JP, Mandel JA. Tensile Strength of Concrete Affected by Uniformly Distributed and Closely Spaced Short Lengths of Wire Reinforcement. JP 1964;61:657–72. https://doi.org/10.14359/7801.
[42] Aveston J, Kelly A. Theory of multiple fracture of fibrous composites. J Mater Sci 1973;8:352–62. https://doi.org/10.1007/BF00550155.
[43] Stroeven P. Stereological Principles of Spatial Modeling Applied to Steel Fiber-Reinforced Concrete in Tension. MJ 2009;106:213–22. https://doi.org/10.14359/56545.
[44] Alberti MG, Enfedaque A, Gálvez JC. A review on the assessment and prediction of the orientation and distribution of fibres for concrete. Compos B Eng 2018;151:274–90. https://doi.org/10.1016/j.compositesb.2018.05.040.
[45] Lee S-C, Cho J-Y, Vecchio FJ. Diverse Embedment Model for Steel Fiber-Reinforced Concrete in Tension: Model Development. MJ 2011;108:516–25. https://doi.org/10.14359/51683261.
[46] Ng TS, Htut T, Foster S. Fracture of Steel Fibre Reinforced Concrete – The Unified Variable Engagement Model. Sydney, Australia: School of Civil and Environmental Engineering, The University of New South Wales; 2012.
[47] Voo JYL, Foster S. Variable Engagement Model for the Design of Fibre Reinforced Concrete Structures. Advanced Materials for Construction of Bridges, Buildings, and Other Structures III 2003.
[48] Mudadu A, Tiberti G, Germano F, Plizzari GA, Morbi A. The effect of fiber orientation on the post-cracking behavior of steel fiber reinforced concrete under bending and uniaxial tensile tests. Cem Concr Compos 2018;93:274–88. https://doi.org/10.1016/j.cemconcomp.2018.07.012.
[49] Abrishambaf A, Barros JAO, Cunha VMCF. Relation between fibre distribution and post-cracking behaviour in steel fibre reinforced self-compacting concrete panels. Cem Concr Res 2013;51:57–66. https://doi.org/10.1016/j.cemconres.2013.04.009.
[50] Ferrara L, Di Prisco M, Lamperti MGL. Identification of the stress-crack opening behavior of HPFRCC: the role of flow-induced fiber orientation. FraMCoS, vol. 7, Jeju, Korea: 2010, p. 1541–50.
[51] Hudson JA, Brown ET, Fairhurst C. Optimizing the control of rock failure in servo-controlled laboratory tests. Rock Mech 1971;3:217–24. https://doi.org/10.1007/BF01238181.
[52] Hudson JA, Crouch SL, Fairhurst C. Soft, stiff and servo-controlled testing machines: a review with reference to rock failure. Eng Geol 1972;6:155–89. https://doi.org/10.1016/0013-7952(72)90001-4.
[53] Bernard E. Influence of Test Machine Control Method on Flexural Performance of Fiber Reinforced Concrete Beams. J ASTM Int 2009:6. https://doi.org/10.1520/JAI102327.
[54] Plummer AR. Control techniques for structural testing: A review. Proceedings of the Institution of Mechanical Engineers, Part I: Journal of Systems and Control Engineering 2007;221:139–69. https://doi.org/10.1243/09596518JSCE295.
[55] Muttoni A. Die Anwendbarkeit der Plastizitätstheorie in der Bemessung von Stahlbeton 1990:158 S. https://doi.org/10.3929/ETHZ-A-000569822.
[56] Bažant ZP. Instability, Ductility, and Size Effect in Strain-Softening Concrete. J Engrg Mech Div 1976;102:331–44. https://doi.org/10.1061/JMCEA3.0002111.
[57] Salamon MDG. Stability, instability and design of pillar workings. Int J Rock Mech Min Sci Geomech Abs 1970;7:613–31. https://doi.org/10.1016/0148-9062(70)90022-7.
[58] Khalifa J. Limit Analysis and Design of Reinforced Concrete Shell Elements. Department of Civil Engineering, University of Toronto; 1986. PhD thesis.
[59] Kirschner U, Collins MP. Investigating the Behaviour of Reinforced Concrete Shell Elements. Publication no. 86-09. Department of Civil Engineering, University of Toronto, 1986.
[60] Yap B. Behaviour of Ultra High Performance Fibre Reinforced Concrete Subjected to Pure Shear. Thesis 2020.